Urban Climate 67 (2026) 102961

Contents lists available at ScienceDirect

Urban Climate

journal homepage: www.elsevier.com/locate/uclim

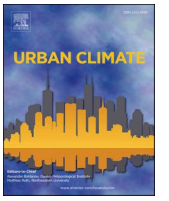

Microclimate monitoring and modelling in a regenerating urban environment: Milano (Italy)

Luca Gallia [a,*], Stefano Basiricò [a], Shamila Haddad [b,c], Thomas Parkinson [b], Aysu Kuru [b,c], Akisha Nomoto [b], Roberto Colombo [a], Riccardo Castellanza [a], Federico Agliardi [a]

[a] Department of Earth and Environmental Sciences, University of Milano-Bicocca, Milan, Italy
[b] School of Architecture, Design and Planning, The University of Sydney, Sydney, Australia
[c] Sydney Net Zero Institute, The University of Sydney, Sydney, Australia

ARTICLE INFO

Keywords:
Urban Heat Island
Urban climate
Microclimate
Air temperature
Surface temperature
Modelling
Thermal comfort

ABSTRACT

Urban regeneration projects in densely populated areas often involve limited, small-scale interventions. The present study provides a data-driven evaluation of solutions to mitigate the urban heat island effect at microscale, integrating densely distributed multisensory and multitemporal monitoring, material characterization, and microscale modelling. A dedicated monitoring system was utilized to measure microclimatic variables during the various phases of regeneration of a compact public square in Milan (Italy). The observations were utilized to establish boundary conditions and to calibrate and validate a microclimatic numerical model for a typical summer day. Three configurations representing different stages of regeneration were analyzed: pre-regeneration conditions, post-regeneration, and a future planned condition. The results obtained from the study indicate that changes in near ground air temperature were limited, whereas surface temperatures and radiative conditions exhibited clearer contrasts linked to the optical and thermal properties of materials and to shading. Reflective paving reduced surface heating in some locations but did not improve mean radiant temperature under peak solar exposure, with local increases that may penalize pedestrian comfort. The findings of this study suggest that the most significant reductions in radiative heat load and the most marked improvements in thermal comfort are produced by mature tree shading. This highlights the importance of optimizing shade placement relative to pedestrian-use areas and of considering soil moisture and maintenance. The objective is to provide support in optimizing mitigation strategies in regeneration projects, highlighting positive aspects and critical points in the distribution of solutions designed to benefit both the microclimate and pedestrian comfort.

1. Introduction

Urbanization is increasing worldwide and cities are becoming more exposed to heat related impacts. As urban areas expand and densify, the modification of land cover and the accumulation of heat in built environments often lead to higher temperatures compared to surrounding rural areas, a phenomenon commonly referred to as the Urban Heat Island (UHI; Oke, 1982). UHI related temperature

* Corresponding author.
E-mail address: l.gallia@campus.unimib.it (L. Gallia).

https://doi.org/10.1016/j.uclim.2026.102961
Received 23 January 2026; Received in revised form 24 April 2026; Accepted 18 May 2026
Available online 10 June 2026
2212-0955/© 2026 The Authors. Published by Elsevier B.V. This is an open access article under the CC BY license (http://creativecommons.org/licenses/by/4.0/).

differences can affect environmental conditions and human health, with direct implications for outdoor thermal comfort and heat related risks (Santamouris, 2020). Since these processes act across multiple spatial scales, understanding and quantifying local thermal conditions is essential to support effective mitigation actions, especially within urban regeneration projects where design interventions are implemented at neighborhood and site scale. In the context of urban regeneration, increasing the albedo of surfaces, de-paving to increase soil permeability, and introducing vegetation or blue bodies (Oke, 2002) are key in mitigation process. Highly reflective materials are commonly considered to obtain "cool surfaces" for pavements and roofs (Giorio and Paparella, 2023). The impact of these solutions is twofold: they influence outdoor temperatures as well as indoor temperatures. Indeed, these solutions result in a decrease in the consumption of energy for the purpose of cooling, which consequently leads to a reduction in greenhouse gas emissions (Santamouris, 2020).

The mitigating effect of increased vegetation cover has been observed on both urban and local scales. Starting from the creation of city parks that form "Cool Islands" in cities, to street trees and vegetation applied to various surfaces either horizontally, ground and roofs or vertically such as building walls. It has been demonstrated that the efficacy of these solutions in reducing temperatures is attributable to three factors: evaporation, transpiration and shading (Han et al., 2023).

The efficacy of mitigation strategies is typically analyzed during the design stage and validated during implementation through a combination of experimental observations and numerical simulations, which together provide a fundamental basis for assessing the potential of individual or combined interventions (Aleksandrowicz et al., 2023; Crank et al., 2018; Krayenhoff et al., 2021). Numerical simulations based on Computational Fluid Dynamics (CFD) play a central role in representing and predicting urban climate processes, with different tools developed for mesoscale and microscale applications. Mesoscale analyses often rely on models such as the Weather Research and Forecasting model (Skamarock and K. J. B., 2024) the Urban Climate Map (UC-Map; Ng, 2015) or UrbClim (De Ridder et al., 2015) whereas microscale studies typically use SOLWEIG (Lindberg et al., 2008), RayMan (Matzarakis et al., 2007) or PALM-4 U (Maronga et al., 2020; Lobaccaro et al., 2021; Vieira Zezzo et al., 2023). SOLWEIG efficiently estimates Mean Radiant Temperature (MRT) but has limited flexibility for complex or dynamic urban settings, while RayMan rapidly calculates MRT and comfort indices such as PMV (Predicted Mean Vote) and SET* (Standard Effective Temperature), using default parameterizations that reduce computational effort but at the cost of lower spatial accuracy (Meng et al., 2025). PALM-4 U, a LES-based system, is increasingly adopted for its ability to explicitly resolve turbulence and incorporate detailed urban-physics modules; however, its implementation requires extensive parameterization and substantial computational resources, which limits its applicability in real-world urban projects where many input data are difficult to quantify (Matzarakis et al., 2007; Vogel et al., 2022).

Among microscale models, ENVI-met (Bruse and Fleer, 1998) is considered one of the leading tools for fine-scale urban climate modelling (Lobaccaro et al., 2021). This tool was selected because it allows specific prescription of surface and soil properties, the three-dimensional representation of vegetation and solves radiative exchanges in a three-dimensional urban domain, which is suitable for comparing paving materials and vegetation configurations in microscale mitigation assessments (Tsoka et al., 2018; Lobaccaro et al., 2021). Its application has been employed in a wide range of climatic and urban contexts, including the Mediterranean area and Italy.

In Lombardy region in Italy, existing studies reflect these broader tendencies. Perini and Magliocco (2014) employed idealized block models driven by meteorological inputs representative of different Italian cities, while Ciacci et al. (2023) analyzed the retrofitting of a single industrial building using a proxy structure due to limited local information. These contributions provide valuable insights but do not address ongoing regeneration processes or incorporate in-situ microclimatic measurements. Owing to its rapid urban expansion, high population density and extensive built-up fabric, Milan has long been a relevant case for investigating the urban heat island phenomenon. Early studies date back to the early 1980s, with seminal work by Bacci and Maugeri (1992). Subsequent research applied a range of methods based on satellite imagery, in situ monitoring and modelling to characterize UHI intensity (Borghi et al., 2000; Pichierri et al., 2012; Anniballe et al., 2014; Puche et al., 2023).

Despite the extensive use of field observations and numerical simulations in urban climate research, a gap remains between research assessments and real, feasible regeneration projects, partly because evidence-based design requires reliable modelling tools and transparent evaluation practices, which are not always available or consistently applied (Tsoka et al., 2018; Aleksandrowicz et al., 2023). In this context, microscale simulations often rely on assumed or database default surface optical properties, even though discrepancies between measured and default albedo values for common materials have been documented in the literature (Aleksandrowicz et al., 2023; Eingrüber et al., 2024). These discrepancies can directly affect reflected shortwave radiation and surface temperature patterns and therefore influence radiative conditions that are relevant for heat stress (Tsoka et al., 2018; Aleksandrowicz et al., 2023). Furthermore, studies that explicitly measure surface parameters *in situ* demonstrate that real values can deviate from literature values after years of environmental exposure, which has direct implications for parameterization choices in applied modelling (Eingrüber et al., 2024). Moreover, modelling studies emphasize the importance of evaluating model performance against field data, and they indicate that comparisons made at clearly defined, matching measurement locations are particularly effective in strengthening model evaluation (Song and Park, 2015). Finally, synthesis work on ENVI-met evaluation highlights that model performance and uncertainty depend strongly on parameterization choices and on the availability of suitable validation data, thus reinforcing the need for transparent input specification and measurement-informed model evaluation in applied project settings (Tsoka et al., 2018; Aleksandrowicz et al., 2023). In this context, we focus on the combination of dense, high-resolution environmental monitoring data with microscale numerical simulations to quantify the microclimatic effects of a real urban regeneration project. In the Po Valley, and in Milan in particular, published ENVI-met applications remain limited and have often relied on idealized model domains rather than real case studies (Perini and Magliocco, 2014) or have required proxy representations due to restricted access to site specific information (Ciacci et al., 2023). In our approach, simulations are based on measured material properties, and model outputs are validated using in-situ data. By considering a relatively small but complex area across different stages of urban

regeneration, the study aims at quantifying the impacts of surface materials and vegetation cover changes on the local microclimate and thermal comfort. Finally, our study aims at discussing the potential of high-resolution multi-parameter monitoring to support the entire workflow of urban regeneration projects. In this context, the present study combines dense, high-resolution environmental monitoring with microscale simulations to quantify the microclimatic effects of a real urban regeneration intervention. By examining a compact public space across different regeneration phases, the study assesses how changes in surface materials and vegetation establishment affect key microclimatic variables and outdoor thermal comfort. Furthermore, it discusses practical implications and limitations relevant to similar constrained projects.

2. Methodology

2.1. Microscale urban regeneration: Piazza della Scienza

The Metropolitan City of Milan (Fig. 1) comprises 133 municipalities over an area of approximately 1575 km^2 and has a resident population of more than three million inhabitants. Geographically, the Metropolitan City of Milan lies in the central-western sector of the Po Valley, a wide alluvial basin bounded by the Alps to the north and the northern Apennines to the south, a configuration that favors weak atmospheric ventilation, pollutant accumulation and frequent temperature inversions (ARPA, 2014; ISPRA, 2023). According to the Köppen–Geiger climate classification (Kottek et al., 2006; Peel et al., 2007), Milan has a warm temperate, fully humid climate with hot summers (Cfa), characterized by hot and humid summers and cold winters.

In this framework, Piazza della Scienza (Fig. 1, right), situated in the central-eastern sector of the Bicocca district (Milan, Italy), was constructed between 1990 and 2000. The square is framed by four university buildings hosting scientific departments, which together define a square layout. The C-shaped buildings are oriented to approximately 21 degrees east of true north and extend over eight floors in total, with five above ground and three underground, reaching a height of approximately 32 m. The buildings are separated at their eastern and western ends to allow tram circulation along the east–west axis, while they are connected along the north–south axis by an elevated bridge beginning at the second floor. At each of its four corners, lowered courtyards located 4.5 m below street level contain limited green areas with grass and three mature trees per courtyard. These, together with twelve Magnolia trees along the tramway, constitute the only substantial vegetated elements within the square (Fig. 2). Indeed, the square consisted almost entirely of self-locking concrete pavers.

Since 2023, the square has been included in a new urban-regeneration project promoted by MUSA (Multilayered Urban Sustainability Action) initiative (part of the National Recovery and Resilience Plan - PNRR – Next Generation EU). Thus, Piazza della Scienza has been undergoing extensive urban regeneration since June 2023. Of the square's total surface of approximately 10.000 m^2, the project currently covers about 8.000 m^2, focusing exclusively on interventions at ground level.

The project involved the complete removal and replacement of the previous pavement with the introduction of new paving materials and landscaped areas composed of shrubs and trees. The new pavement includes gneiss cubes (Luserna stone) and granite slabs. The latter delineate the edges of the Luserna stone paving and form a continuous pedestrian path connecting the two newly created green spaces. The trees planted are mainly *Acer Campester* and *Acer Cissifolium*, deciduous trees that can reach heights of over 10 m with an oval, rounded crown of 6 m wide (Podaras, 1996; Nagy, 2004), while the shrubs are various species that reach heights of 50 cm.

Since the initial phase of work commenced in June 2023, the existing pavement has been entirely removed, a process that was completed in September 2023. Concurrently, the new paving was laid, starting from one quadrant at a time, with work concluding in September 2024.

This intervention, aimed at improving environmental, social and aesthetic conditions, also provides a valuable opportunity to test an integrated methodology combining on-site monitoring and microclimate modelling to support the design of UHI mitigation

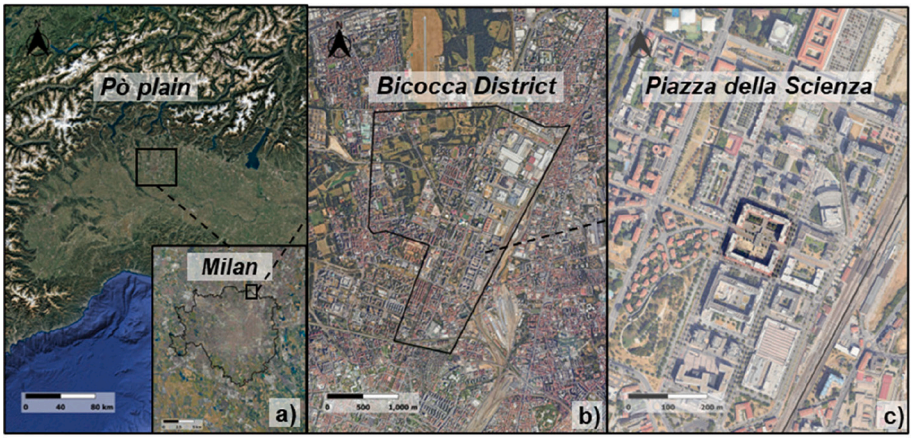

Fig. 1. Study area location. a) northern Italy and Milan b) Bicocca District and c) Piazza della Scienza (45°30′48“ N, 9°12’38” E) located in Bicocca District, Milan (Italy).

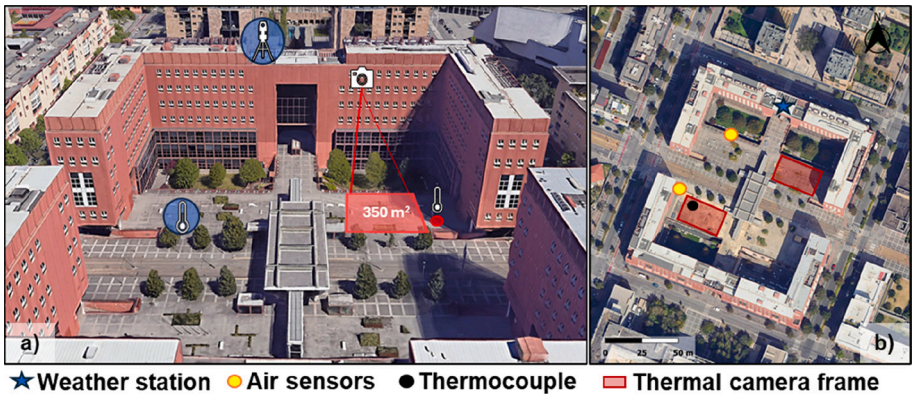

Fig. 2. Monitoring network. Visual representation of the network of monitoring devices placed in Piazza della Scienza a). Thermal camera shots of the two diametrically opposite sides of the square (red rectangles) and layout of the air temperature sensors (yellow dots) and surface temperature sensors (black dot) b). (For interpretation of the references to colour in this figure legend, the reader is referred to the web version of this article.)

strategies within the broader framework of urban regeneration. Although the regeneration project had been defined prior to the start of this study, the ongoing transformation of Piazza della Scienza offers a unique opportunity to assess its microclimatic implications. The findings can inform future adjustments and complementary design actions, strengthening the development of climate-responsive strategies within the evolving regeneration process.

2.2. *Experimental characterization and long-term monitoring*

Since the present study aims at evaluating the impact of an urban regeneration project through a quantitative approach integrating monitoring data and numerical modelling, a microscale monitoring network was designed to capture local microclimatic conditions and their main drivers throughout the regeneration process (Fig. 2). Land surface temperature (T_{surf}) and near-surface air temperature (T_a) were measured together with incoming solar radiation, relative humidity, and wind speed and direction, which control the surface energy balance and provide input to the microclimate model. Finally, air temperature measured above roof level provides an upper boundary condition for the urban canopy layer and a reference for interpreting near-surface observations.

Fig. 2b shows the instrumentation position forming the field monitoring network, consisting of portable sensors strategically located across various points in the square. Throughout the regeneration process, the monitoring strategy followed a multi-temporal and multi-sensor approach (Fig. 3). Near surface air temperature was continuously recorded at fixed stations and with HOBO data loggers, providing long-term time series at selected locations. At daily and sub-daily scales, time-lapse InfraRed Thermography (Vollmer and Mollmann, 2008) was used to monitor T_{surf} over the study area. Furthermore, T_{surf} has been recorded with thermocouple fixed to the ground surface. The technical specifications of all instruments used are summarized in Table 1.

The monitoring locations have been selected to be representative of the main surface types and exposure conditions in the square. At the same time, we have taken steps to ensure stable, long-term deployment. The thermal camera viewpoint was selected to include, within a single frame, representative areas of both pre- and post-regeneration materials. Was not intended to provide full spatial coverage of the entire site, but rather to support surface temperature monitoring and to validate the modelled surface temperature over the main surface types. Additionally, the fixed-point T_a and relative humidity sensors were strategically positioned to sample contrasting microclimatic conditions in the square, including locations with different levels of solar exposure and shading patterns caused by the surrounding buildings, the tram canopy and vegetation. In the final placement, practical constraints such as mounting feasibility and reducing disturbance risk were also taken into consideration.

This combination of measuring devices provided data with complementary temporal resolution and spatial coverage, which were jointly used to measure surface and air temperature, the relevant forcing variables, and the boundary conditions of the site. Table 1 reports spatial and temporal characteristics of various instruments involved.

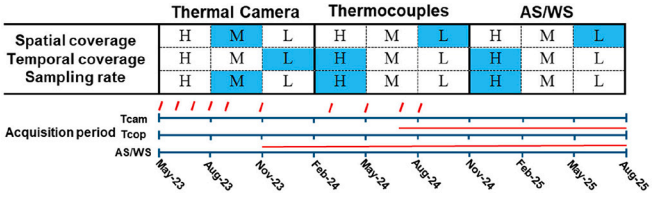

Fig. 3. Instruments' temporal and spatial coverage characteristics. H = High, M = Medium, L = Low.

Table 1
Air temperature and surface temperature instruments specifications..

Weather Station Davis Vantage Pro2	
T_a/RH Resolution	0,1 °C / 1%
Wind speed/direction Resolution	0.1 m/s / 1°
Operating range	−40 to +65 °C
T_a/RH accuracy	0,5 °C / 3%
Wind speed/direction accuracy	1 m/s / 3°
Onset HOBO - MX2301A	
T_a/RH Resolution	0.02 °C / 0.01%
Operating range	−40° to 70 °C
T_a/RH accuracy	± 0.25 °C / ± 2.5%
FLIR T1020 thermal camera	
Spectral range	7.5 to 14 μm
Operating range	- 40 to +50 °C
T_{surf} Accuracy	± 1°C
T_{surf} Sensitivity	0.02 °C
Onset HOBO - UX120-014 M / Type-T Thermocouple	
T_{surf} Sensitivity	0.02 °C
Operating range	−20° to 70 °C
T_{surf} accuracy	±0.6 °C / ±1,0 °C

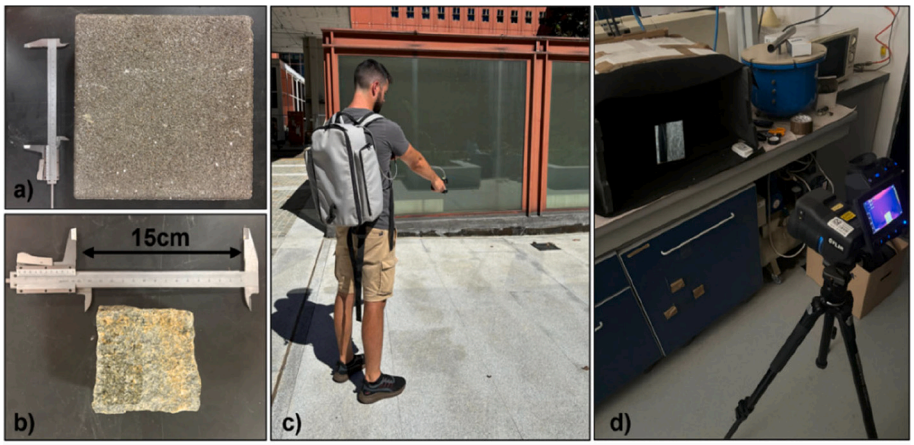

Fig. 4. Material characterization. Pavement material and method to retrieve their thermophysical and optical properties. Old pavement material, interlocking concrete pavers a). New pavement material, Luserna cubes b). Emissivity retrieval process c). Albedo measurements on granite slabs d).

2.2.1. *Material characterization*

The square pre- and post-regeneration characteristics are defined by the presence of three distinct types of impermeable materials and permeable areas. Specifically, prior to the regeneration, the square was predominantly paved with interlocking concrete pavers (Fig. 4a), alongside small patches of permeable soil covered with grass. Following the intervention, the surface was replaced with Luserna stone cubes (Fig. 4b) and granite slabs (Fig. 4c). The latter are primarily distributed between two landscaped areas, creating a pedestrian path connecting them. These materials differ significantly in their thermophysical properties.

2.2.1.1. Surface albedo. Broadband albedo (α) was derived from measurements obtained using a portable spectrometer (Fig. 4c) and following the formulation proposed by Aoki et al. (2011).

$$\alpha = \frac{\int_{\lambda_1}^{\lambda_2} r(\lambda)F(\lambda)d\lambda}{\int_{\lambda_1}^{\lambda_2} F(\lambda)d\lambda}$$

where $r(\lambda)$ represents the spectral reflectance of the surface and $F(\lambda)$ is the incident spectral solar flux at the surface. Field radiance measurements were collected on 26 September 2024 at 12 PM under clear sky conditions, using the Spectral Evolution SR-3500 (Haverhill, MA, USA), which covers the visible to shortwave infrared spectrum (300–2500 nm). Albedo values were collected for different surfaces, including both the new and pre-existing pavement materials in the square.

2.2.1.2. Surface emissivity. The surface emissivity was derived indirectly (Datcu et al., 2005; Vollmer and Mollmann, 2008; Mineo and Pappalardo, 2021) by using the FLIR T1020 thermal camera (Fig. 4d). Three representative surface samples, corresponding to the different types of impermeable materials in the square, were analyzed. Each sample was heated in a laboratory oven to a known

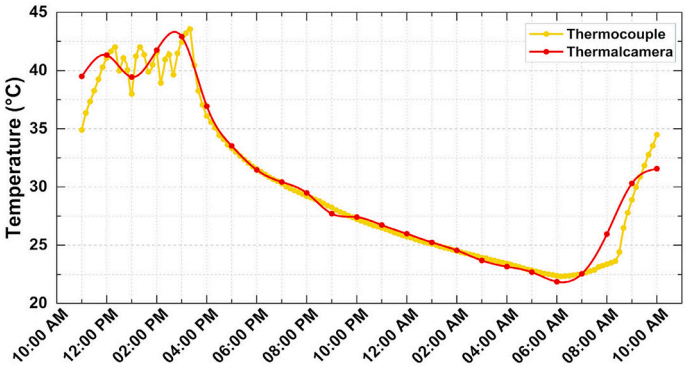

Fig. 5. Comparison between thermal imaging camera and thermocouple data over a summer day, namely 05 July 2024.

temperature of 70 °C. A piece of black insulating tape with known emissivity of 0.97 (Mineo and Pappalardo, 2021) was applied to the surface of each sample. By comparing the measured radiative temperatures of the samples with the reference tape, and adjusting for ambient and reflected temperatures, the emissivity of each material was determined.

2.2.2. *Weather variables*

A Davis Vantage Pro2 weather station (WS) was employed to record environmental atmospheric parameters. The instrument is located on the roof of the university building, at an elevation of approximately 32 m (Fig. 3). The Integrated Sensor Suite (ISS) measures air temperature (T_a, °C) and Relative Humidity (RH, %), as well as wind speed (m/s), wind direction (deg) and Global Horizontal Solar Radiation (GHI, W/m^2). The sensor has been installed since June 2022 and acquires data every ten minutes.

Additionally, two Onset HOBO MX2301A dataloggers were installed to monitor T_a and RH. The sensors were positioned at a height of 3 m above ground (Fig. 3, yellow dots) and equipped with radiation shields to prevent direct solar exposure from affecting the accuracy of the readings. In accordance with WS data, the sensors have been collecting data at 10-min intervals since November 2023. The technical specifications of all instruments used are summarized in Table 1.

2.2.3. *Surface temperature*

Surface temperature (T_{surf}) was measured using InfraRed Technique, specifically with a FLIR T1020 thermal camera. The camera was positioned on the fourth floor of the university building to capture thermal images of a portion of the square at an angle as close to perpendicular to the ground as possible (Fig. 3). The acquisition of images was conducted over the course of several months, from June 2023 to August 2024. Specifically, the images were collected at a frequency of 20 min over 24-h periods, with clear-sky condition, to document both diurnal heating and nocturnal cooling phases. The captured area corresponds to approximately 350 m^2, including surfaces representative of both pre- and post-regeneration conditions. Each acquisition has been made with clear-sky condition.

Furthermore, a T-type thermocouple was installed on a HOBO UX120-014 M datalogger within the thermal camera frame (Fig. 3). The contact measurements were obtained during the first week of July 2024 and employed to validate the data acquired by the thermal camera.

As demonstrated in Fig. 5, a robust correlation exists (RMSE = 1.35, MAE = 0.9) between the data obtained directly by the thermocouple and the indirect data obtained by the thermal camera. This positive correlation serves to strengthen the thermal camera data, which was subsequently utilized to validate the model outputs.

2.3. *Numerical model*

Numerical simulations were performed to evaluate the microclimatic conditions of Piazza della Scienza using ENVI-met (Bruse and Fleer, 1998), a widely recognized and validated model for urban environmental analysis (Toparlar et al., 2017; Tsoka et al., 2018). ENVI-met is a three-dimensional, non-hydrostatic model that adopts a holistic approach to simulate the interactions between atmospheric processes, soil, vegetation, and built structures.

ENVI-met software includes several modules to manage projects, generate the model domain, set simulation parameters, execute runs, and visualize results. Additionally, the input of material properties and three-dimensional vegetation characteristics is carried out through dedicated modules (Bruse, 2004a). A one-dimensional (1D) component extends from ground level up to 2500 m and is used to apply boundary conditions to the primary three-dimensional (3D) model. Additionally, a 1D/3D soil model is included. At the core of ENVI-met is the atmospheric module, which solves the Reynolds-averaged, non-hydrostatic Navier–Stokes equations using Computational Fluid Dynamics techniques and combines sub-models to calculate the other variables as air temperature and humidity, turbulence and radiative fluxes (Huttner, 2012). The typical horizontal resolution in simulation is 1 to 10 m with a typical simulated time interval of 1–5 days. This tool was selected in this study due to its capability to simulate micro- and neighborhood-scale processes (Detommaso et al., 2021), its comparatively user-friendly interface and the generally accessible nature of its input data.

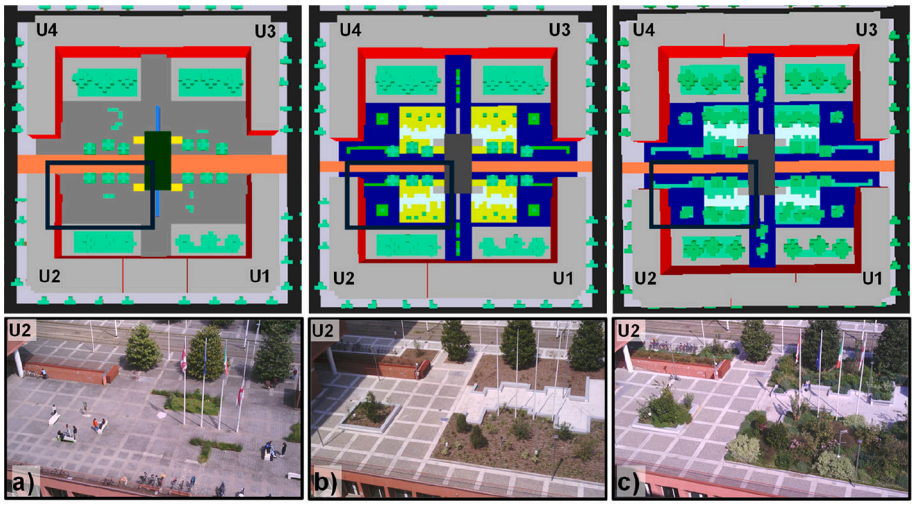

Fig. 6. Simulated scenarios. The three different scenarios S0 – Pre-regeneration a), S1 – Post-regeneration b) and S2 – Post-regeneration (Growing Season) c) exploited to simulate environmental conditions in Piazza della Scienza.

2.3.1. Model set up

The model domain was designed to accurately reflect the geometric and geographic features of the study area (Fig. 6 and Fig. 7). Grid cells were set to dimensions of 2 × 2 × 2 m to balance spatial detail and computational efficiency while still providing reliable results (Abdollahzadeh and Biloria, 2021; Salata et al., 2016). The domain includes Piazza della Scienza and a surrounding buffer zone of 130 m to North, 150 m to East, 190 m to South and 100 m to West (Fig. 7a), which serves a dual purpose: capturing the influence of nearby buildings on airflow and minimizing boundary errors that could affect the accuracy of results within the square. The domain

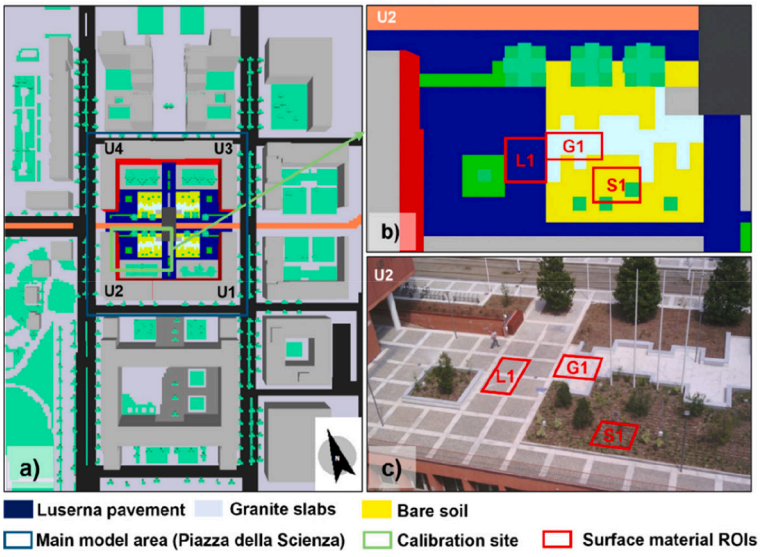

Fig. 7. Reference validation scenario. Whole domain Scenario S1 reproduced in ENVI-met a). Modelled U2 quadrant used as model evaluation site; the different colours represent the new ground surfaces after the square regeneration b). RGB image of U2 quadrant c).

Table 2
Scenarios characteristics summarized..

	Regeneration phase	Paving / surfaces	Vegetation
S0	Pre-intervention	Dark-grey concrete blocks	12 Magnolia trees, small green patches
S1	Post-intervention (End of works)	**Luserna cubes (L1)** and **granite slabs (G1) / flowerbeds (B1)**	New plantings in flowerbeds (B1) **small**, **bare soil**
S2	Future condition	Same as S1	Mature vegetation

Table 3
Simulation information for model validation and scenarios comparison.

Simulation settings	
Start simulation day (dd.mm.yyyy)	30/07/2024
Start simulation time (hh.mm.ss)	05:00:00
Total simulation time in hours (h)	24
Output timestep (min)	60
Meteorological inputs	
Wind speed [m/s]	2
Wind direction [◦]	150
Air Temperature T_a [°C]	Hourly data from weather station
Relative Humidity RH [%]	Hourly data from weather station
Soil inputs	
Upper layer (0–20 cm) [°C]	20
Middle layer (20–50 cm) [°C]	20
Deep layer (50–200 cm) [°C]	18

Type of Pavement	Albedo	Emissivity	Volumetric heat capacity $\frac{J}{(m^3K)}*10^{-6}$	Heat conductivity (w/mK)
Concrete	0.15	0.98	2.08[a]	1.63[a]
Luserna	0.25	0.97	1.75[a]	2.33[a]
Granite	0.47	0.96	2.34[a]	3.10[a]
Tram line	0.25[a]	0.95[a]	2.00[a]	1.00[a]

[a]Software default value.

grid is defined in a cartesian plane with square cells; this configuration allows the import of georeferenced bitmap images that can be rotated to align with the orientation of the site. This ensures the accurate representation of solar exposure and wind directions relative to building geometry. This configuration resulted in a computational grid of 178 × 236 × 40 cells (including the buffer zone), covering a plan area of 168,032 m^2, with a total simulation domain volume of 13,442,560 m^3. Each simulation started at 5 AM to capture pre-sunrise conditions. All environmental inputs, except solar radiation, were taken from the WS. Wind speed and direction were kept constant (2 m/s and 150 deg., Table 3) and were chosen to represent conditions of low wind speed during the central hours of the analyzed day, while air temperature and relative humidity were updated hourly from measurements. Wind speed and direction were kept constant, while air temperature and relative humidity were updated hourly from measurements. All other environmental inputs, except solar radiation, were taken from the WS.

Three urban regeneration scenarios were simulated (Fig. 6): the square before the regeneration intervention (S0), at the end of intervention work, i.e. post -regeneration (S1), and in a future (planned) condition corresponding to the stage at which the newly planted vegetation is fully established (S2).

Scenario S0 (Fig. 6a) presents a square surface predominantly covered with dark grey concrete blocks with vegetation limited to twelve Magnolia trees located in the central area adjacent to the tramway.

Scenario S1 (Fig. 6b) is characterized by different materials and new flowerbeds. Fig. 7b-c shows a quadrant of the entire site, where grey Luserna stone cubes (L1) and nearly white granite slabs (G1) are reported. To accommodate grid resolution limitations, granite slabs were included only between the flowerbeds (Fig. 7c). In addition, shrubs and trees such as field maples were planted in flowerbeds (B1), though their small size at the time left much of the surface bare (Fig. 7b).

Scenario S2 (Fig. 6c) shares the same ground surface layout as S1 but includes mature vegetation, reflecting the intended long-term effect of the regeneration intervention and the growing season state of the square. In this configuration, the flowerbeds are modelled with dense low vegetation approximately 50 cm in height and 28 fully developed trees reaching around 8 m. Tree size was selected based on a realistic growth constraint for the site, namely the thin soil and pruning. Moreover, each tree was parameterized with a crown width of approximately 6 m and treated as deciduous; for the analyzed summer period the canopy was set to full leaf conditions using the standard model deciduous summer setting (Podaras, 1996; Nagy, 2004). The height was selected based on what the tree could realistically reach due to the thin soil and pruning.

The main characteristics of each scenario are presented in Table 2.

As illustrated in Fig. 6 certain regions or structural elements within the model remain unaltered across all scenarios. The orange line, oriented Est-West, corresponds to the tramway, which is surrounded by twelve Magnolia trees that were not involved in the regeneration projects. In the central area, the tram stop shelter (dark green) and the staircase (light blue and yellow) are located. The latter elements facilitate access to the University building via the basement. Following the completion of the regeneration work, the four underground courts at the corners of the square remained unchanged, despite their inclusion in the project plan. This deviation was attributed to complications during the construction process.

The three representations of the model in Fig. 6 are accompanied by RGB images of quadrant related to building name U2. The images presented here illustrate the condition of the square on which the development of the scenarios was based. Given the symmetry of the square and the concurrent progression of the works across all areas, quadrant U2, as depicted in the images, can be considered a representative sample of the entire square.

2.3.2. Model calibration / validation

S1 (Fig. 7) was considered as the reference scenario for model calibration and testing, corresponding to the square configuration at the end of regeneration works and selected due to the largest availability of T_{surf} and T_a monitoring data. The model was calibrated on a selected day (30 July 2024), representative of the hottest days of the year in Milan, characterized by clear sky conditions, very low wind speed and high solar forcing, which is known to exert a major influence on surface temperatures (Bruse, 2004b; Detommaso et al., 2021). Model calibration was performed by testing alternative meteorological forcing options and wind settings for the reference day. Measured pavement albedo and emissivity were kept fixed as model inputs, and thermophysical parameters not measured in this study were retained as ENVI-met default values (Table 3). Model performance was evaluated at three test areas corresponding to different surface materials (L1, G1 and B1) using T_{surf} observations, and using the average simulated T_a at 3 m above ground compared with the mean of the two HOBO sensors positioned at the same height.

For each simulation, calibration performance was evaluated by comparing the measured and simulated values of T_a and T_{surf}, since these are the parameters best simulated by the model (Acero and Arrizabalaga, 2018). To do so, Root Mean Square Error (RMSE) and Mean Absolute Error (MAE; Tsoka et al., 2017; Detommaso et al., 2021) statistics were selected.

2.4. Thermal comfort evaluation with different tools

Thermal comfort was assessed using two complementary approaches: the BIO-met module included in the ENVI-met software and the Advanced Berkeley Comfort (ABC) model (Huizenga et al., 2001; Zhang et al., 2010a, 2010b, 2010c).

For the ENVI-met simulation, the Physiological Equivalent Temperature (PET; Gagge and Nishi, 1972) was calculated. PET is based on the two-node model proposed by Gagge and Nishi (1972), which balances body heat flows through radiation, convection, evaporation, and metabolism. The index was selected on the basis that, among the range of comfort indices available within ENVI-met, it is best suited to the assessment of outdoor thermal comfort. The input data for BIO-met module are derived from numerical simulations, specifically the output variables of atmospheric conditions.

To complement this evaluation, and to compare the results of two different tools, the ABC model has been utilized. The Advanced Berkeley Comfort Model, itself derived from Slowijk's classic thermoregulation scheme (Stolwijk and Hardy, 1966), has been further developed to incorporate key improvements, including detailed body segmentation, multilayer tissue representation, and a refined hemodynamic model with countercurrent heat exchange. In contrast to conventional indices, such as PET, the ABC model integrates physiological variables with perceptual predictors, thereby enabling the estimation of both local and whole-body thermal sensation and comfort.

The ABC model necessitates the consideration of several key atmospheric variables to ensure its functionality. These were obtained directly from the outputs of the ENVI-met simulations.

2.4.1. Thermal comfort set-up

Thermal comfort analysis was performed, considering the experience of a pedestrian crossing the square where the path is composed of four stops, each lasting 10 min (Fig. 14 and Fig. 15). This time duration is consistent with recent in situ monitoring protocols that utilize this time window to capture sequential microclimatic variability in pedestrian areas (Mendes et al., 2025). This duration is also important because it ensures that thermal perception can stabilize before comfort assessment (Jing et al., 2024) and is representative of short exposures in urban transit contexts, where typical dwell times are often below 15 min (Piselli et al., 2018).

This analysis based on the path is intended as an assessment with high temporal resolution during peak heat conditions, rather than a complete characterization of the day in terms of comfort. The selection of stops was determined by the variation in pedestrian exposure to solar radiation. In scenarios S0 and S1, the shaded areas are confined to the initial and final stops, with shades generated by structures such as the building and the tram canopy. In scenario S2, however, the second stop on the path is located under the shade provided by mature trees.

With regard to the assessment of comfort using ENVI-met, the PET values were extracted from the maps corresponding to a height of 1.4 m. In contrast, the ENVI-met assessment provides the diurnal evolution and the spatial distribution of comfort across the entire square.

The ABC model accurately reproduces thermal comfort using variables acquired over a short period of time. For this reason, the comfort analysis based on the path was performed by coupling ENVI-met outputs with the ABC model. ENVI-met maps were saved at hourly intervals for the purpose of spatial visualization, whereas four receptors were positioned at each stop to extract point time series at one-minute resolution. These receptor outputs were then used as input variables for the ABC calculation for the selected time window from 2 PM to 2:40 PM, which corresponds to one of the hottest periods of the day.

Other inputs, such as the demographic characteristics of the subject and their clothing, were kept standard for both tools involved. In particular, a 35-year-old male subject was utilized as a model. The clothing insulation values, for a summer clothes type, refer to those proposed by the study by Lee et al. (2013).

3. Results

3.1. Long term in-situ monitoring results

Fig. 8 shows various monitoring acquisitions carried out during the project phases. Prior to the intervention (Fig. 8a, S0 scenario), the concrete block paving (C) registered surface temperatures of approximately 55 °C at 3 PM, whereas the small permeable grassy

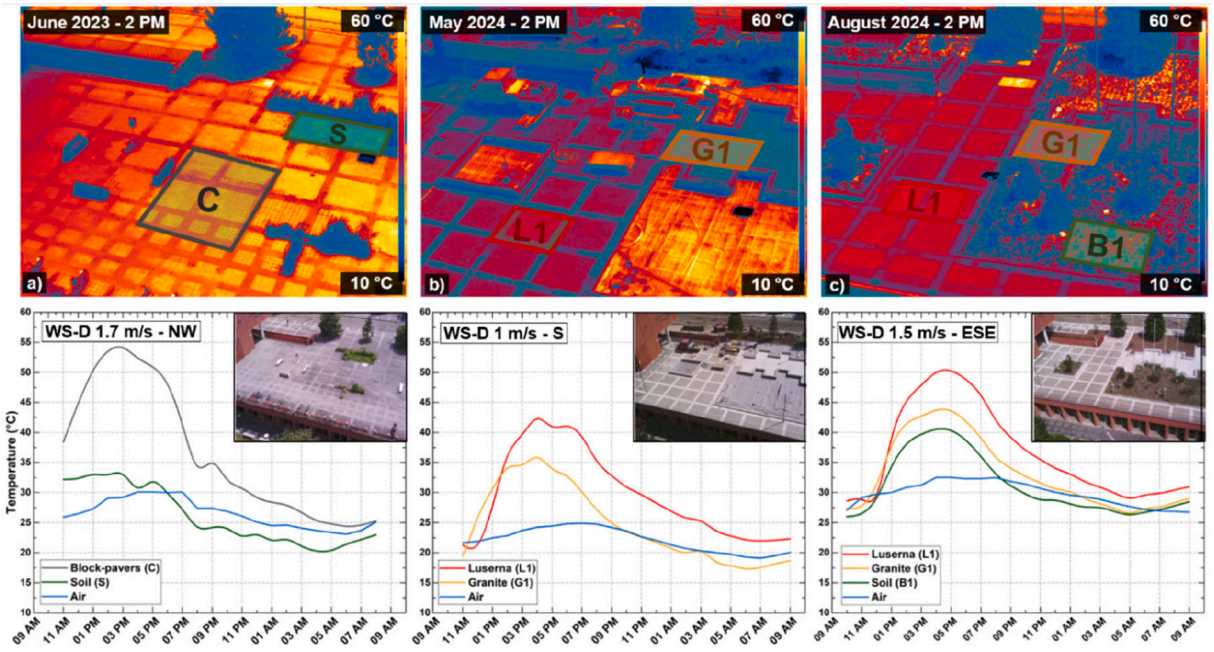

Fig. 8. Monitoring results. Thermal images were acquired during the work phases. The thermal images are presented for comparisons of surface types within a single day; direct quantitative comparison between years under different meteorological conditions is not intended. The graphs below show the T_{surf} measurements for the day, with information on T_a, wind speed and direction (WS-D). Image acquired on 20 June 2023 at 2 PM pre-regeneration (S0 scenario, a), image acquired on 1 August 2024 at 2 PM (Scenario S1, c).

area (S) exhibited a maximum temperature of about 32.5 °C. However, after 6 PM, the temperature over the vegetated area exhibited a rapid decline, remaining below the air temperature throughout the night.

In May, during the intermediate phase of the works, the new paving had already been installed (Fig. 8b). The maximum T_{surf} was recorded at approximately 42.5 °C at 4 PM on the Luserna stone (L1). Granite (G1) recorded a consistent temperature difference of approximately 5 °C from 12 PM onwards, with a subsequent drop in surface temperature below the T_{air} (20 °C) after 2 AM. The areas of the thermal image that exhibit the highest temperatures correspond to the zones that had been designated for the installation of permeable soil, although these plans had not yet been executed at that time. In conclusion, the August acquisition (Fig. 8cFig. 9c), which was conducted shortly following the completion of the works (S1 scenario), indicates that Luserna stone (L1) reached a maximum of 50 °C at 5:30 PM, with T_{surf} above 40 °C until midnight. Granite (G1) exhibited a comparable diurnal pattern; however, it remained 8 °C cooler during the afternoon and 5 °C cooler for the rest of the day.

Bare soil in the new flowerbeds (B1) exhibited lower temperatures than the paved surfaces, but still reached values close to 40 °C, becoming cooler than the air temperature (≈32.5 °C) after 8:30 PM.

3.2. *Validation of reference scenario*

Among the tested configurations, the combination of basic meteorology and the meteorological input and the material parameters reported in Table 3 minimized errors (RMSE/MAE) across the calibration targets, indicating the most robust model setup.

As illustrated in Fig. 9a, the model tends to overestimate T_a values during the first half of the day, up to 6 PM, and underestimate them afterwards. This behavior has been reported in other validation studies as well (Yang et al., 2013; Middel et al., 2014; Acero and Herranz-Pascual, 2015; Tsoka et al., 2018). Overall, the agreement represented by the RMSE and MAE values is high (1.36 °C and 1.16 °C, respectively) and the R^2 value is 0.72.

When compared with reference values reported in the literature (Piselli et al., 2018), the model demonstrates acceptable performance. Both RMSE and MAE fall below the median values presented by (Tsoka et al., 2018) which are 1.51 °C and 1.34 °C, respectively, while R^2 is only slightly lower than the typical median value of 0.92.

T_{surf} (Fig. 9b) is accurately reproduced by the model during the morning and early afternoon for L1. However, a slight underestimation is observed from 5 PM onwards. The Root Mean Square Error (RMSE) and Mean Absolute Error (MAE) for L1 are 2.30 °C and 2.12 °C, respectively, with an R^2 of 0.97, indicating a strong correlation between observed and simulated data.

A similar trend is evident for G1, where underestimation begins at 5 PM and continues through the evening, as well as between 1 PM and 4 PM. Despite this, the overall agreement remains high, with RMSE and MAE values of 1.45 °C and 1.35 °C, respectively, and an R^2 of 0.98.

In the case of B1, the model overestimates surface temperatures during the hottest part of the day (11 AM to 4 PM), likely due to the model's inability to simulate intermittent irrigation that occurred on-site during this period, at midday and even at nighttime at 3 AM.

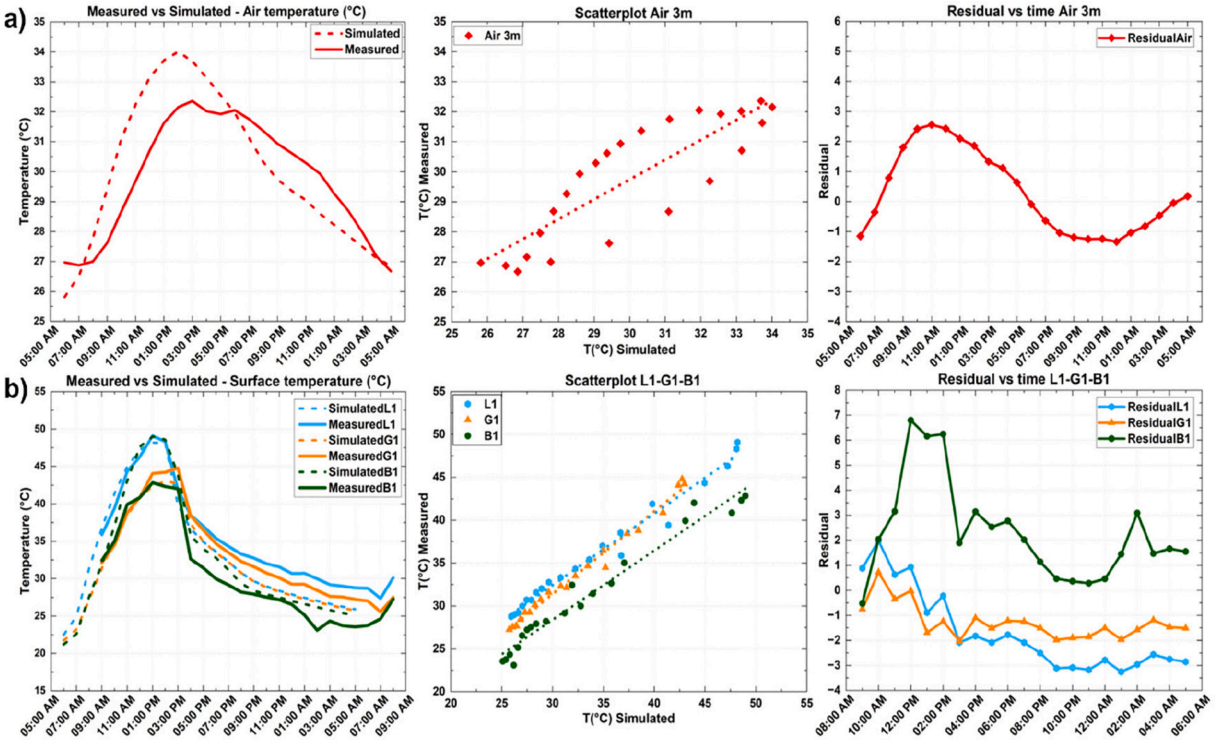

Fig. 9. Calibration plots. Air temperatures simulated vs measured data above a) and surface temperatures simulated vs measured data below b), with their scatterplots and residual vs time plots.

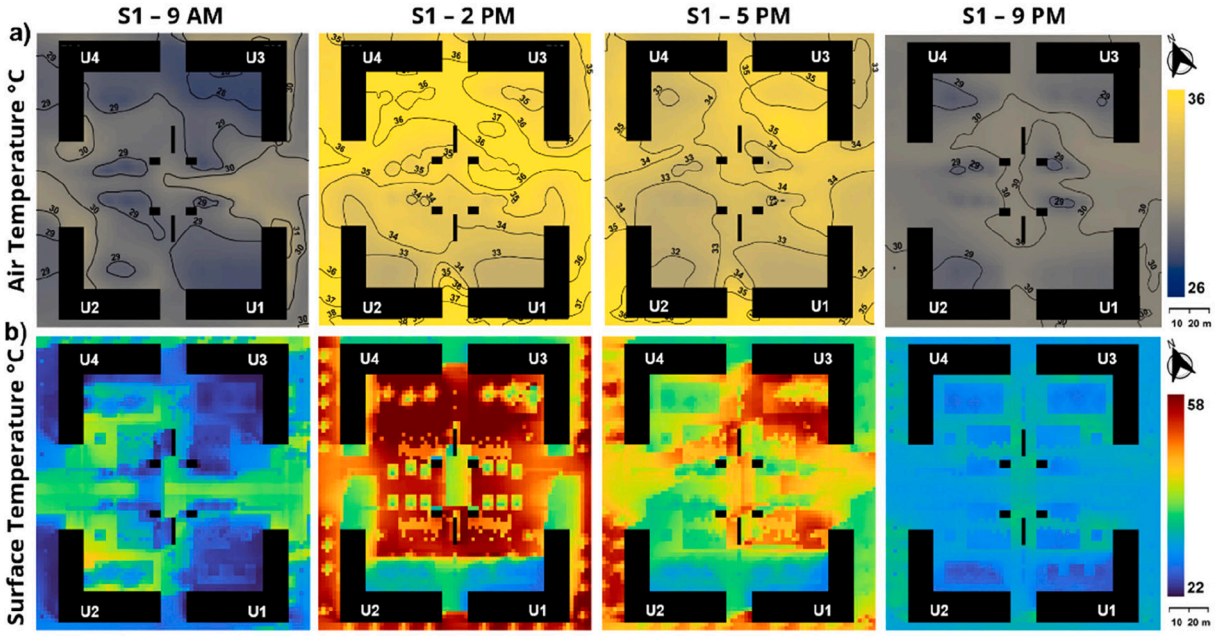

Fig. 10. Daily temperatures distribution. Ta distribution at four different hours of the day (Top line a). Bottom line represents Tsurf distribution at the same time b).

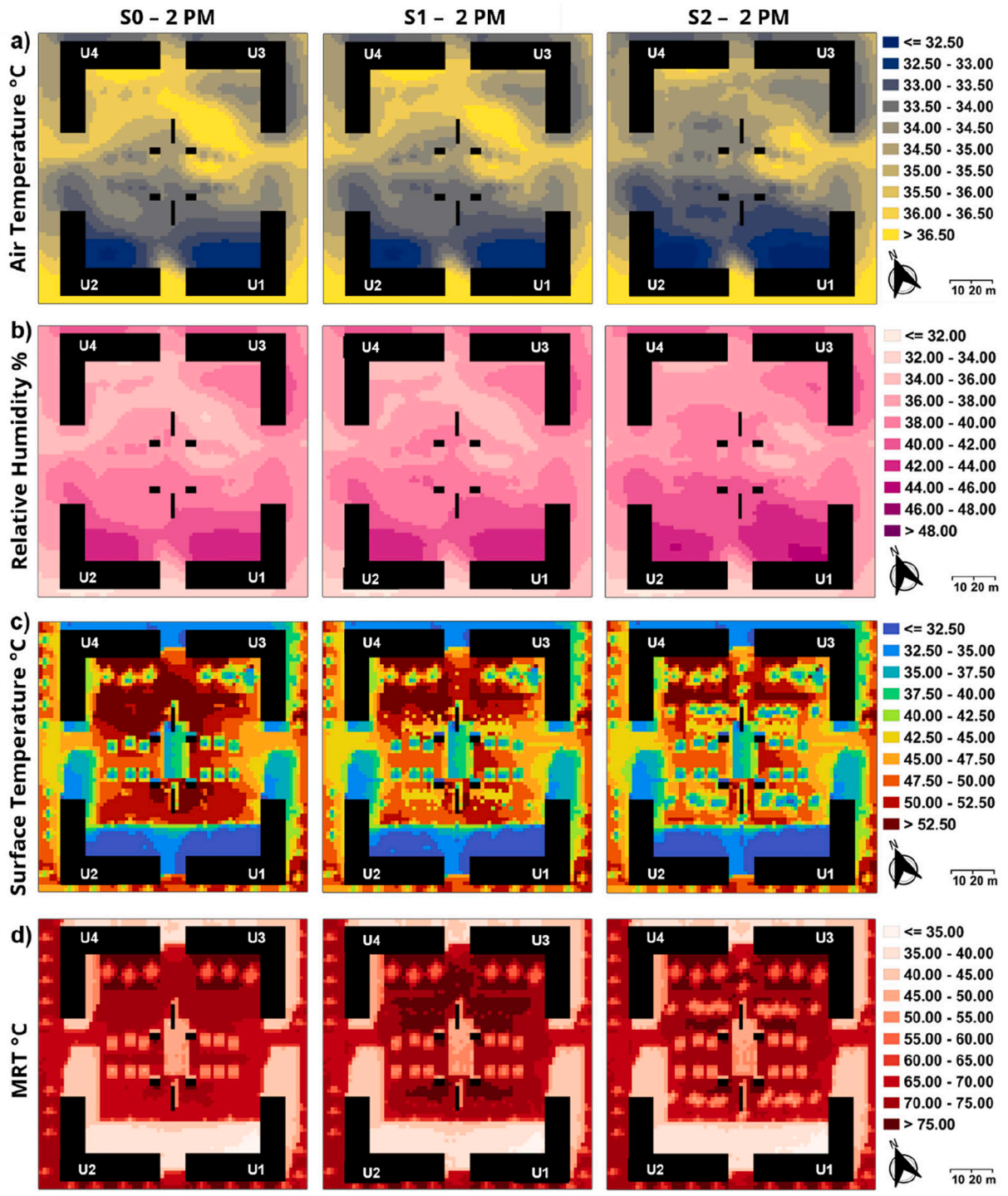

Fig. 11. Scenarios comparison. The maps show the distribution of T_a (a), RH (b), T_{surf} (c) and MRT (d), at the same time for scenarios S0, S1 and S2.

However, the temporal patterns between measured and simulated values are consistent. The corresponding RMSE and MAE are 3.01 °C and 2.34 °C, respectively, with an R^2 of 0.96. Although relatively few studies have used surface temperature to validate ENVI-met, the R^2 values obtained in this study are near the upper end of the range (0.6 to 0.97) reported in the literature (Tsoka et al., 2018).

3.3. Scenario-based simulations

To observe daily temperatures variation, T_a and T_{surf} maps (Fig. 10) of reference scenario S1 were analyzed at four different times of the day, namely 9 AM, 2 PM, 5 PM and 9 PM.

T_a maps (Fig. 10 top line *a*) are presented at 1 m above ground level. The eastern portion of Piazza della Scienza is largely shaded due to the orientation of the buildings and their relative position to the sun. At 9 AM, air temperature across the square is approximately 29 °C, with values ranging from 27.7 °C to 30.8 °C. The coolest areas are found near the eastern facades and around the central Magnolia trees, where shading and the presence of vegetation contribute to localized cooling effects. At 2 PM, corresponding to the peak of solar radiation, shading is confined to a few limited areas. Air temperatures rise significantly, ranging from 32.4 °C to 37.2 °C. The northern sector of the square records the highest values, while slightly lower temperatures are observed along the southern edge, particularly near buildings U1 and U2. This gradient reflects differences in solar exposure and shading patterns, which are strongly influenced by the square's geometry and its 21° rotation from the north. By 5 PM, a moderate reduction in air temperature is detected, with values ranging from 31.6 °C to 35.8 °C. The western area appears to be the coolest at this hour, likely due to increased shading in the late afternoon. At 9 PM, after sunset, the thermal gradient within the square becomes less pronounced. The difference between the minimum and maximum values is reduced to approximately 3 °C. The lowest air temperatures are concentrated near the central vegetation and at the corners of the buildings, indicating a residual cooling effect associated with the shaded and vegetated zones, and reduced thermal inertia in these microenvironments.

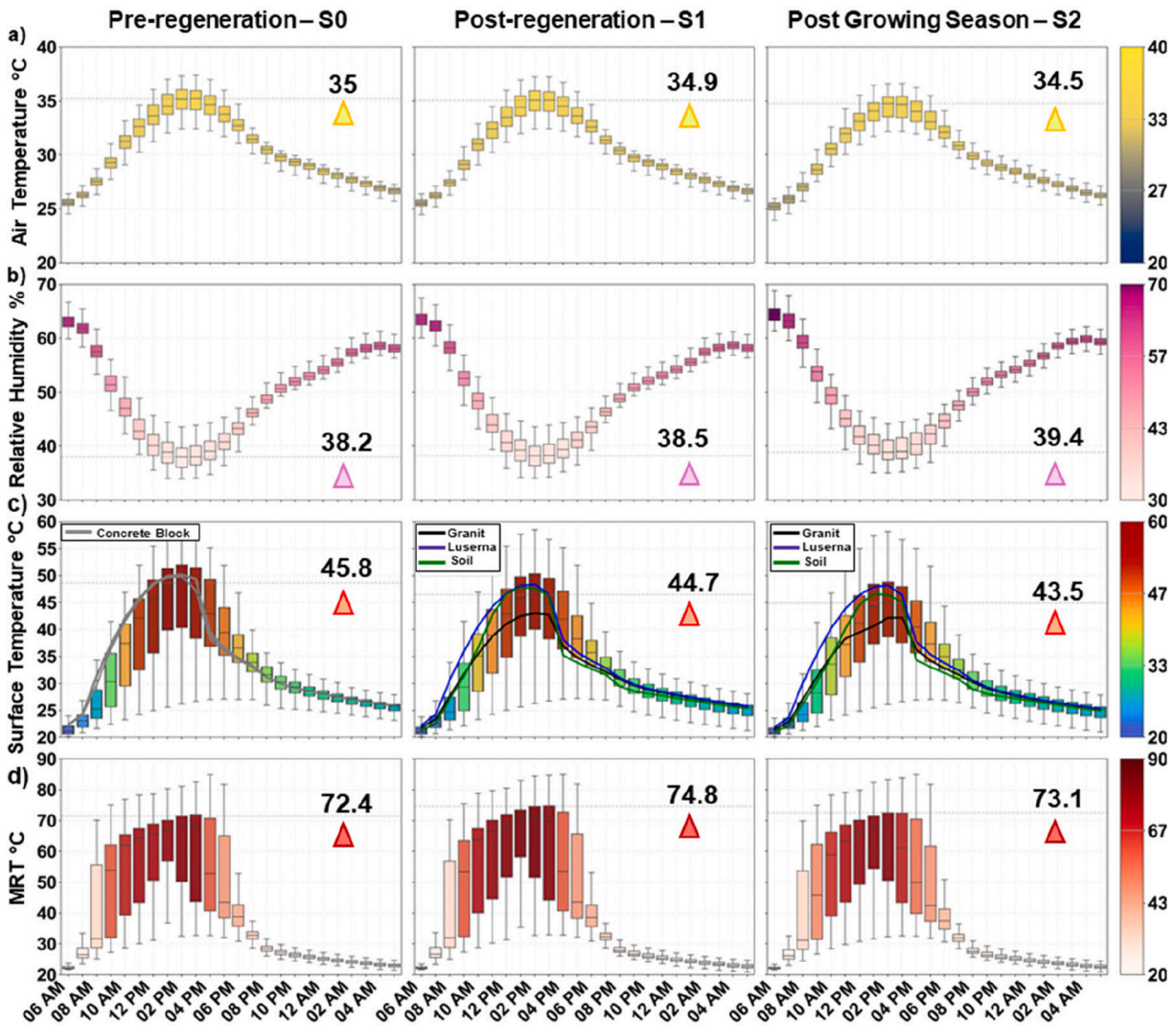

Fig. 12. Boxplot representation of T_a (a), RH (b), T_{surf} (c) and MRT (d), throughout the day for scenarios S0, S1 and S2. The lines in surface temperatures (c) graphs represent the different surfaces within the squares. Temperature values reported in each plot correspond to the maximum value (minimum for RH) of the median that has been simulated over the course of the day.

T_{surf} maps (Fig. 10 bottom line *b*) are presented at the same selected daytime. At 9 AM, following approximately two hours of solar exposure, surface temperatures exhibit significant variation, ranging from 22 to 41.5 °C. In shaded eastern areas, temperatures remain lower than in other regions. On the western side, the lowest recorded temperatures are found in areas of granite slabs and exposed soil, which exhibit minimal heat accumulation during this period. At 2 PM, a marked increase in surface temperatures is observed, ranging from 26 to 58.5 °C. At this time, shadows are minimal, and thermal contrasts are pronounced. Granite surfaces have been found to demonstrate consistently lower temperatures than the other surfaces, particularly in areas situated beneath Magnolia trees. This phenomenon can be attributed to the material properties of granite itself, including higher reflectance, as well as the impact of vegetation shading. At 5 PM, a slight decrease in surface temperatures is observed, from 27 °C to 51.9 °C. The eastern side, still exposed to solar radiation, exhibits higher values, particularly in Luserna-paved areas. In contrast, the bare soil zones on the western side cool more rapidly. At 9 PM, the absence of solar radiation results in a more homogeneous surface temperature distribution, with differences reduced to around 9 °C. The bare soil patches were found to be the coldest surfaces at this time, indicating faster heat loss compared to mineral paving.

Overall, no clear spatial correspondence emerges between surface temperature patterns driven by paving materials and air temperature at pedestrian level during the day. Areas with lower T_{surf} over more reflective paving do not show systematically lower T_a. Cooler T_a is mainly observed where shading from vegetation and buildings reduces solar exposure.

For a comparative analysis of the three scenarios, a single time of day was selected, with the most extreme conditions occurring during daylight hours; Fig. 11 presents the model output maps for 30 July at 2 PM. The four variables analyzed, namely T_a, RH, T_{surf} and the bio-meteorological parameter Mean Radiant Temperature, were selected since they are among the key variables affecting outdoor thermal comfort (Abdollahzadeh and Biloria, 2021; Olivieri et al., 2024). T_a, RH and MRT maps were computed at a height of 1 m.

The spatial distribution of air temperature (Fig. 11*a*) appears similar in both S0 and S1 scenarios, with values ranging from 32.4 °C to 37.3 °C. In the S2, cooler zones become more widespread, particularly on the western side of the square. The overall temperature range shifts slightly, with the minimum decreasing to 32.1 °C and the maximum dropping to 36.6 °C. These modest changes suggest a localized cooling effect attributable to increased vegetation and associated shading.

The distribution of relative humidity (Fig. 11*b*) in S0 and S1 shows similar patterns, with only minor localized reductions in the central area. In contrast, S2 reveals a more extensive and uniform increase in relative humidity, especially across the central and southern portions of the domain. This behavior is consistent with the combined effect of evapotranspiration and lower air temperatures, both of which contribute to higher RH at pedestrian height.

The most pronounced differences between scenarios emerge in surface temperature distributions (Fig. 11*c*). Scenario S0, in paved areas exposed to solar radiation, presents a homogeneous pattern, with values ranging between 47.5 °C and 50 °C, consistent with the uniform surface properties. In both S1 and S2, surface temperatures remain high in areas paved with Luserna stone, similar to those observed in the dark concrete blocks of S0. However, granite slabs consistently exhibit lower temperatures, with reductions of up to 5 °C compared to the pre-regeneration and adjacent Luserna areas. In S2, the presence of vegetation becomes clearly visible, with temperature reductions of approximately 7 °C in vegetated soil zones and up to 10 to 12 °C in areas shaded by tree canopies.

MRT shows a different response (Fig. 11*d*). Compared with S0, S1 does not provide an improvement in MRT under peak solar exposure, and localized increases can occur over highly reflective paving. In S2, substantial reductions are evident beneath mature tree cover, with differences reaching about 25–30 °C in fully shaded areas. This highlights the dominant role of tree shading in reducing radiative heat load at pedestrian level.

The comparison of maps allows capturing the spatial patterns of different parameters across the square. However, by extracting the data for each cell, it is possible to obtain a general comparison between the three scenarios for the selected parameters. The extraction cells under consideration are those that fall within the area enclosed by the four buildings. Fig. 12 shows the diurnal variation of the four key parameters previously analyzed, represented through boxplots for the three simulated scenarios.

The plots capture both the temporal trends and the internal variability of microclimatic conditions across Piazza della Scienza. These results provide insight into how differences in surface materials and vegetation influence the overall thermal environment throughout the day.

Air temperature at 1 m height (Fig. 12*a*) shows limited variation between scenarios. In Scenario S1, the introduction of new paving materials and bare soil yields only minor reductions compared to the Pre-regeneration.

The maximum difference between the median values occurred at 11 AM, reaching 0.2 °C, while after 7 PM, the differences remain below 0.2 °C. In S2, where vegetation has reached full maturity, a more persistent cooling effect is observed. Temperature differences exceed 0.37 °C for most of the day, with the greatest reduction, approximately 0.6 °C, occurring at 5 PM. These findings suggest that the presence of vegetation contributes to modest but continuous reductions in near-ground air temperature during the hottest hours.

Relative humidity at 1 m height (Fig. 12*b*) follows a similar temporal pattern across all scenarios. Absolute differences are consistently below 1.8%, a value that falls within the typical accuracy range (±2%) of standard outdoor sensors. Given this limited variation, relative humidity was not considered a critical factor for further microclimatic evaluation in this case.

As shown in Fig. 12*c*, surface temperature demonstrates the highest variability both temporally and spatially. This is attributed to the heterogeneous distribution of shading from buildings and vegetation, as well as the varying thermal properties of ground surfaces. The greatest difference between S0 and S1 is observed at 11 AM, with a maximum drop of mean temperature of 1.5 °C. The highest surface temperatures occur in the early afternoon, when solar forcing is strongest. S2 consistently exhibits lower surface temperatures than the Pre-regeneration. Reductions surpass 2.2 °C for most of the day, with a maximum difference of approximately 2.6 °C recorded around midday.

Mean radiant temperature at 1 m height (Fig. 12*d*) also shows notable variability, particularly during early morning and late

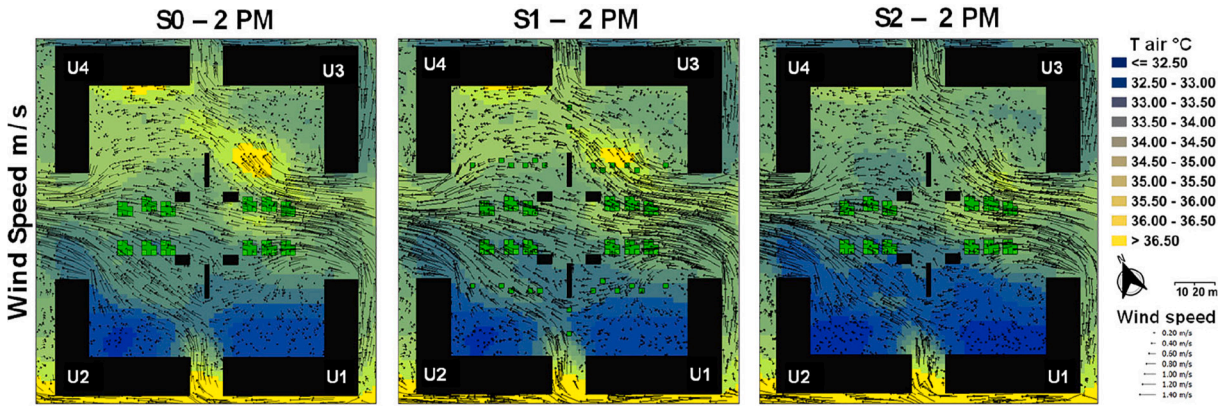

Fig. 13. The wind flow has been overlaid on the T air map. The wind and air temperature map is referenced at a height of 1 m and at 2 PM for the three scenarios.

afternoon hours, when parts of the square remain shaded. This variability reflects the complex radiative exchanges between urban surfaces and the human body, including possible direct solar exposure (Aleksandrowicz et al., 2023). Scenario S1 does not improve mean radiant temperature compared to the Pre-regeneration; rather, the use of high-albedo granite paving appears to increase MRT values throughout the day. In Scenario S2, the presence of mature vegetation contributes to substantial reductions in mean radiant temperature, especially in shaded zones. These findings underline the critical role of vegetation in mitigating radiant heat load and enhancing outdoor thermal comfort for pedestrians.

Finally, it is significant to observe the variation in surface behavior throughout the day. The lines shown in Fig. 12*c* represent the temperature trends of different materials, by selecting three points (L1, G1 and B1) with the same location in the three scenarios. In the first scenario, the surface remains constant, and the trend is applicable to the three points under consideration. In the second case, it is evident that the granite curve attains lower Tsurf values, even when compared to the bare soil. The latter has been shown to exhibit a

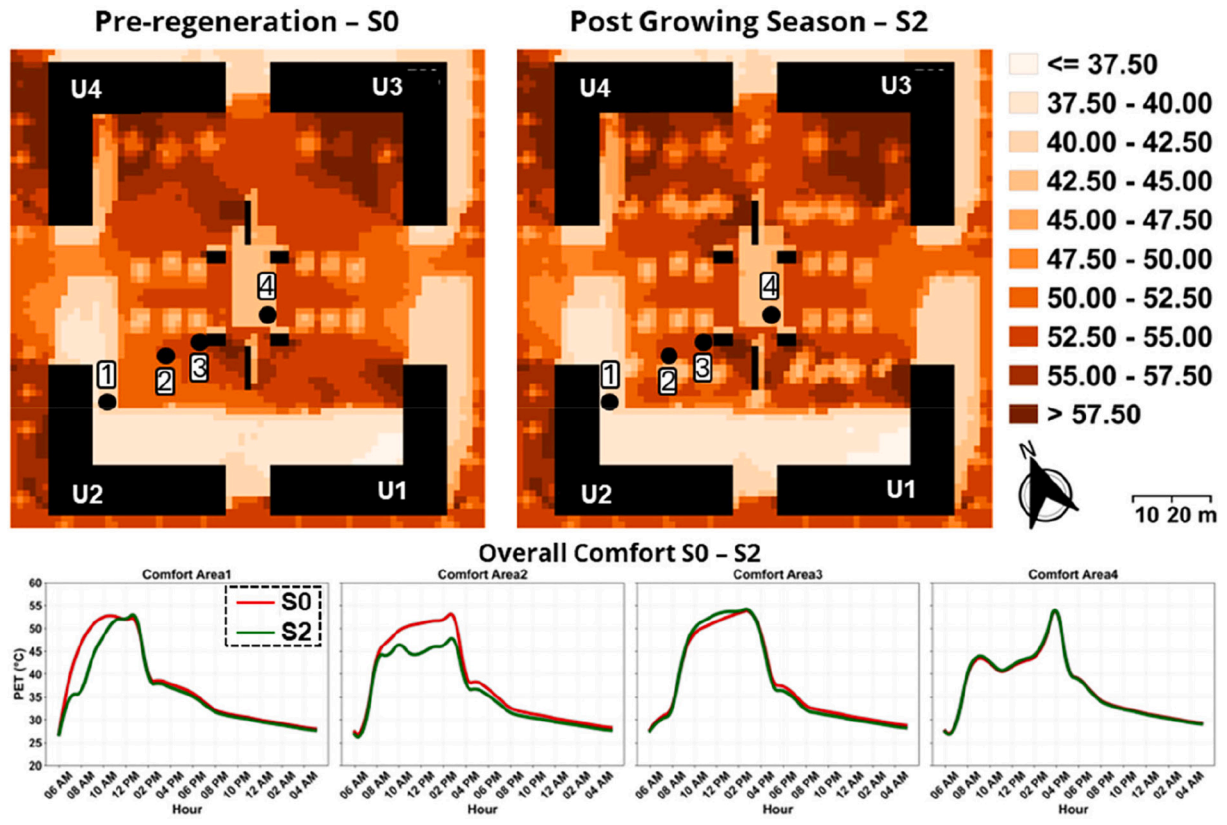

Fig. 14. Diurnal variation of the Physiological Equivalent Temperature (PET) at four receptors for the three simulated scenarios.

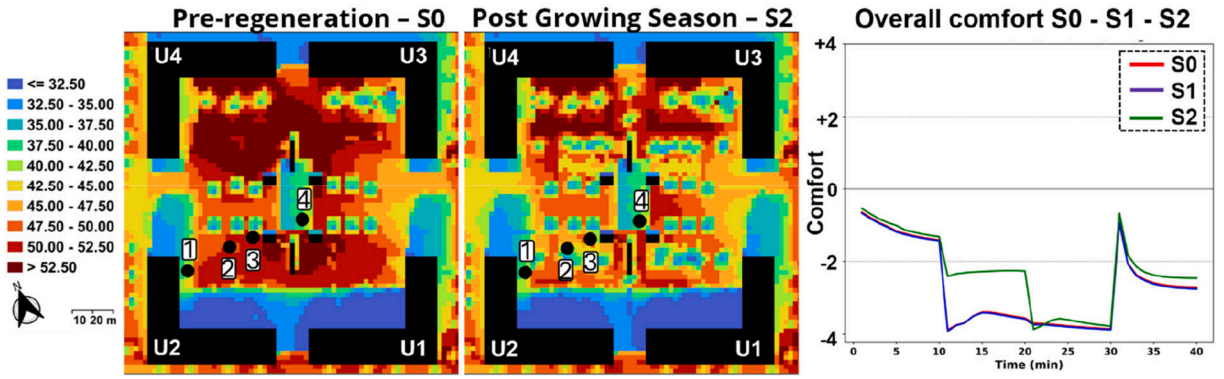

Fig. 15. ABC model. The maps illustrate surface temperatures pre-work and post-work scenarios with mature vegetation, where the points at which thermal comfort is measured are visible. The following three graphs illustrate the overall comfort levels in each scenario. The values ranging from −4 to +4 express comfort, with −4 representing the most uncomfortable condition (very uncomfortable) and + 4 representing the most comfortable condition (very comfortable).

slower heating and faster cooling phase than impermeable surfaces yet still reach temperatures similar to those of Luserna at peak times. In the third scenario, characterized by denser vegetation on soil, the temperature remains lower than in Luserna, although it is higher than in granite.

Wind is a key factor in influencing the microclimate and thermal comfort (Salata et al., 2016). As shown in Fig. 13, the wind flow at a height of 1 m is overlaid on the air temperature map (1 m height) at 2 PM for the three scenarios. Within the confines of the square, the areas in proximity to the buildings and the corners of the square exhibit low speeds ranging from 0.4 to 0.8 m/s. The central east-west channel, the flow is slightly attenuated, with speeds in a range between 1.5 and 1.8, which is similar to those at the entrance and exit of the square. Furthermore, wind maps (Fig. 13) suggest a qualitative spatial consistency between the simulated wind field and the air temperature pattern.

The transition from S0 to S1 exhibits minimal alterations in wind patterns, suggesting that surface materials and the presence of exposed flower beds have negligible effects on airflow. In scenario S2, particularly in areas where trees have grown, there is a slight decrease in wind speed compared to the two previous scenarios. In both the northern and southern regions, the areas with lower wind speed also coincide with locally different air temperature.

3.4. Thermal comfort analysis

As shown in Fig. 14, in the pre-regeneration condition (S0), PET peaks around 3 PM, exceeding 45 °C at the most exposed locations, corresponding to conditions of extreme thermal stress. The implementation of high-albedo paving (S1) produces only a modest reduction, up to 2 °C, in central areas, with peak discomfort persisting during the early afternoon hours. Conversely, the scenario with mature vegetation (S2) exhibits a substantial attenuation of PET, with peak values reduced by 4–6 °C during the hottest period of the day and a faster cooling in the evening. This improvement reflects the combined influence of tree shading and evapotranspiration.

As illustrated in Fig. 15, the four receptors were positioned in the same locations in all scenarios. At the initial stop, which corresponds to 2 PM in the shaded area of the building, the findings suggest the presence of discomfort, which exhibits an increasing trend over the subsequent 10 min. During the second stop, the receptor is fully exposed to solar radiation in scenarios S0 and S1, resulting in a rapid decrease in comfort followed by a slight stabilization, probably associated with short-term a brief stabilization to the new thermal conditions. A divergent outcome is observed in scenario S2, wherein the receptor remains in the shaded area, resulting in superior comfort levels compared to those in S0 and S1. In scenarios S0 and S1, comfort remains low at the third stop under direct sunlight. In contrast, a gradual reduction in comfort is observed in scenario S2. In conclusion, at the fourth stop, which is situated in the shade of the tram shelter, an initial improvement in comfort is observed. However, this is followed by a subsequent decrease in comfort, which then stabilizes at an overall level that is perceived as uncomfortable.

4. Discussion

The present study utilized the redevelopment of Piazza della Scienza, a public square situated on the University of Milano-Bicocca campus in Milan, Italy, as a case study to quantify the microclimatic effects of feasible UHI mitigation measures. This was conducted using a combination of multi-sensor field monitoring and numerical simulations. The monitoring campaign captured the main environmental drivers and response variables, providing a detailed characterization of local conditions and the empirical basis to inform and evaluate the modelling setup. A range of measurements were collected during different phases of the regeneration process. Consequently, the simulations were conducted retrospectively as a post-assessment, rather than as decision support for the project. The numerical analysis focused on the combined introduction of reflective paving materials and new vegetation, comparing the alternative configurations to estimate their impacts on key microclimatic variables and outdoor thermal comfort. In this context, ENVI-met proved

particularly useful because the model structure allows surface types to be parameterized consistently across scenarios. This supported the distinction of the thermal behavior of the different paving solutions introduced by the regeneration project and the interpretation of their implications for surface heating and near-surface conditions. Moreover, the three-dimensional representation of vegetation was crucial for the present study, as it enabled the testing of future scenarios with fully established trees and the capture of the role of shading and radiative exposure on outdoor conditions.

The monitoring campaign was carried out throughout the different phases of the project, allowing the square to be characterized under changing surface configurations and across different seasons. Fig. 8 provides a summary of the monitoring results for the three key stages of the regeneration works. It is notable that in both May (Fig. 8b) and August (Fig. 8c), the paved surfaces reached comparable temperature levels during the morning; however, later in the day, Luserna stone (L1) consistently exhibited higher temperatures compared to granite (G1). This behavior is indicative of the distinct thermal and optical properties of the two materials, which primarily affect surface temperatures.

The simulation results demonstrate minimal variation for the variables examined in the three scenarios. Regarding air temperature, in Scenario S1, the new materials did not lead to significant reductions in air temperature, either in the proximity of the pavement or over the whole square. The biggest decrease of 0.2 °C was observed at 11 AM, in agreement with the range of 0.2–3 °C reported in literature for air temperature reductions associated with reflective materials (Santamouris, 2013; Tsoka et al., 2017). This behavior can be attributed to the limited presence of granite slabs within the area, the surface with higher albedo than previous material. Moreover, no clear spatial correlation was found between areas with higher albedo and localized reductions in air temperature.

Changes in relative humidity were limited in both scenarios; even in S2, increases remained below 2%, consistent with previous work reporting variations as low as 0.32% (Ambrosini et al., 2014). In this context, relative humidity was not found to be a variable strongly affected by mitigation solutions.

Surface temperature showed a more marked response. The simulations confirmed the strong influence of albedo on surface temperature (Tsoka et al., 2018). After the intervention, T_{surf} decreased across the square, and larger increases in albedo led to larger temperature reductions. Granite, which showed an albedo increase of 0.32 compared to the pre-regeneration state, exhibited the largest cooling, whereas Luserna stone, with an increase of 0.10, produced more modest reductions. The recorded decreases were slightly below the 6–12.3 °C range reported by previous numerical studies (Tsoka et al., 2018) but followed the same trend and were consistent with other findings (Piselli et al., 2018). In Scenario S1, bare permeable soil reached relatively high surface temperatures, at times comparable to or higher than those of mineral surfaces, especially granite. This behavior reflects the dry soil conditions assumed in the model. Although the site is irrigated at midday and late night (e.g. 3 AM) the model does not allow partial or time-specific irrigation, thus, soil surfaces remained dry and consequently warm the whole day. This aspect led to the maintenance of high surface temperature and significantly limited decrease in air temperature, as the thermal mitigation performance of grass grid pavers is strictly dependent on adequate water availability (Eingrüber et al., 2024).

In scenario S2, the vegetation in the flower beds was assumed to be fully developed. In this case, air temperature reductions were more evident, due to the combined effect of shading and evapotranspiration, through which vegetation cools the air (Bowler et al., 2010). However, ΔT_a (S0 - S2) remained below 1 °C over the 24-h simulation, in agreement with studies that analyze the combined effect of cool materials and green infrastructure (Castaldo et al., 2017; Piselli et al., 2018). The comparison with S2 highlighted the cooling potential of tree cover: the canopy intercepted incoming solar radiation, limiting heat accumulation at ground level. Differences exceeding 10 °C were observed between exposed and shaded surfaces of identical material, in agreement with the numerical studies that investigated vegetation effects on surface temperature reductions (Piselli et al., 2018; Tsoka et al., 2018).

Mean radiant temperature exhibited strong spatial variability across the square, thereby confirming its dependence on radiative fluxes and material thermal properties (Matzarakis et al., 2010). MRT is highly sensitive to both direct and diffuse solar radiation and is considered a primary determinant of outdoor thermal comfort, especially in conditions of low wind speed (Rosso et al., 2018). The results, particularly those shown in Fig. 10, indicated that high-albedo materials may increase MRT and thus thermal discomfort, in accordance with previous studies (Piselli et al., 2018; Tsoka et al., 2017; Giorio and Paparella, 2023).

Wind advection provides another key element for interpreting the limited and spatially heterogeneous cooling observed in all scenarios. In consideration of the geometry of Piazza della Scienza, the wind flow is concentrated within a preferential corridor. During the day, when temperatures are high, this corridor facilitates the transport of warm air into the square, thereby compensating for part of the local cooling. Consequently, the simulated cooling in S2 remains spatially constrained: cooler air formed in shaded and leeward areas is only weakly exported downwind before being diluted by the dominant inflow. This finding is consistent with other evidence indicating that, in isolated urban spaces, the efficacy of local interventions in reducing near-ground T_a is significantly influenced by advection and urban geometry through channeling driven by temperature and pressure differences (Bartesaghi-Koc et al., 2021).

Vegetation is also essential to balance surface cooling and comfort. As indicated by Salata et al. (2017), tree canopies have the capacity to absorb up to 80% of incoming solar radiation, thereby reducing both shortwave reflections and longwave emissions. The difference in MRT between S1 and S2 reached values of about 25 °C in areas that changed from fully exposed to shaded, within the range of 4–37 °C reported in the literature. However, the overall improvement in MRT in S1 remained limited, and some zones even showed higher values than in S0 as well as for S2compared to S0, despite the increase in shading. The spatial patterns also confirmed the role of shading from adjacent buildings: east-west oriented sector of the square remained consistently warm during peak solar hours due to the lack of shade. The findings on thermal comfort reveal elevated levels of discomfort across all three scenarios. The locations analyzed encompassed sun-exposed and shaded areas, all selected within areas designated for pedestrian passage and rest, in proximity to surfaces with elevated albedo. Consequently, the decrease in direct solar exposure was partially compensated for by an increase in the contribution of reflected shortwave radiation. This increase in radiative load has the potential to compromise the comfort of pedestrians outdoors (Song and Park, 2015; Rosso et al., 2018).

The comfort results should also be interpreted in relation to the boundary conditions of the day analyzed, which is representative of a typical July situation in Milan, characterized by high air temperatures, strong solar radiation and low wind speed. Under such extreme summer conditions, the absence of thermal comfort across the square is consistent with expectations.

Although the study provides useful insights into the microclimatic effects of a real regeneration intervention, some limitations should be acknowledged. The monitoring campaign was aligned with the project timeline, which constrained the amount of pre-intervention data that could be collected before construction started. In addition, the available instrumentation did not include in-situ measurements of wind at pedestrian level and radiative conditions, so a direct validation of near-ground airflow and MRT was not possible. Furthermore, wind forcing was adopted through simplified boundary conditions which may introduce uncertainty under different synoptic situations. Future work would benefit from additional in-situ anemometric and radiative monitoring, a longer pre-intervention baseline when feasible, and the exploration of further alternative scenarios that remain realistic for implementation, including additional shading solutions such as lightweight canopy structures, to support more actionable design choices.

5. Conclusion

Taken together, the findings highlight how the impacts of surface materials and vegetation changes can be accurately quantified with a scenario-based approach to support practical microscale urban regeneration project. In this study, reflective paving resulted in negligible changes in near ground air temperature (e. g. 1 m height). However, under conditions of sun exposure, it led to an increase in MRT, which has a negative impact on pedestrian comfort. However, given the limitations of implementing vegetation uniformly, the design should prioritize the optimal spatial configuration of shading by trees and reflective surfaces. This configuration should target zones with the highest solar exposure and pedestrian use. The effectiveness of planted areas is influenced by soil moisture (Gao et al., 2024) and maintenance, necessitating the consideration of irrigation and soil-management practices in conjunction with layout and material choices.

Although this is a single case study, the results indicate that combining site-specific monitoring with microscale simulations of alternative design scenarios provides a robust basis for comparing regeneration options and interpreting the microclimatic implications of specific choices. This integrated approach is of particular value in real projects where mitigation and comfort goals must be balanced against practical constraints, and where reliable local characterization is essential to reduce the risk of ineffective or counterproductive interventions.

CRediT authorship contribution statement

Luca Gallia: Writing – review & editing, Writing – original draft, Methodology, Investigation, Formal analysis, Data curation, Conceptualization. **Stefano Basiricò:** Methodology, Data curation, Conceptualization. **Shamila Haddad:** Writing – review & editing, Methodology. **Thomas Parkinson:** Writing – review & editing, Methodology. **Aysu Kuru:** Writing – review & editing, Supervision. **Akisha Nomoto:** Methodology. **Roberto Colombo:** Writing – review & editing, Methodology. **Riccardo Castellanza:** Supervision, Conceptualization. **Federico Agliardi:** Writing – original draft, Supervision, Methodology, Data curation, Conceptualization.

Declaration of competing interest

The authors declare that they have no known competing financial interests or personal relationships that could have appeared to influence the work reported in this paper.

Acknowledgement

This work was carried out within the framework of the project *MUSA – Multilayered Urban Sustainability Action* (Project Code ECS000037, CUP H43C22000580001), funded by the European Union – NextGenerationEU under the Italian National Recovery and Resilience Plan (PNRR), Mission 4, Component 2, Investment 1.5 “Ecosistemi dell'Innovazione”, and coordinated by the University of Milano-Bicocca and was partially supported by the Italian Ministry of University and Research (MUR) project “Dipartimenti di Eccellenza 2023–2027, Department of Earth and Environmental Sciences, University of Milano-Bicocca”.

Data availability

Data will be made available on request.

References

Abdollahzadeh, N., Biloria, N., 2021. Outdoor thermal comfort: Analyzing the impact of urban configurations on the thermal performance of street canyons in the humid subtropical climate of Sydney. Front. Architect. Res. 10 (2), 394–409. https://doi.org/10.1016/j.foar.2020.11.006.

Acero, J.A., Arrizabalaga, J., 2018. Evaluating the performance of ENVI-met model in diurnal cycles for different meteorological conditions. Theor. Appl. Climatol. 131 (1–2), 455–469. https://doi.org/10.1007/s00704-016-1971-y.

Acero, J.A., Herranz-Pascual, K., 2015. A comparison of thermal comfort conditions in four urban spaces by means of measurements and modelling techniques. Build. Environ. 93, 245–257. https://doi.org/10.1016/j.buildenv.2015.06.028.

Aleksandrowicz, O., Saroglou, T., Pearlmutter, D., 2023. Evaluation of summer mean radiant temperature simulation in ENVI-met in a hot Mediterranean climate. Build. Environ. 245, 110881. https://doi.org/10.1016/j.buildenv.2023.110881.
Ambrosini, D., Galli, G., Mancini, B., Nardi, I., Sfarra, S., 2014. Evaluating mitigation effects of urban heat islands in a historical small center with the ENVI-Met® climate model. Sustainability 6 (10), 7013–7029. https://doi.org/10.3390/su6107013.
Anniballe, R., Bonafoni, S., Pichierri, M., 2014. Spatial and temporal trends of the surface and air heat island over Milan using MODIS data. Remote Sens. Environ. 150, 163–171. https://doi.org/10.1016/j.rse.2014.05.005.
Aoki, T., Kuchiki, K., Niwano, M., Kodama, Y., Hosaka, M., Tanaka, T., 2011. Physically based snow albedo model for calculating broadband albedos and the solar heating profile in snowpack for general circulation models. J. Geophys. Res. 116 (D11), D11114. https://doi.org/10.1029/2010JD015507.
ARPA, 2014. L'aria che respiro: L'inquinamento atmosferico locale e globale. www.regione.lombardia.it.
Bacci, Maugeri, 1992. The Urban Heat Island of Milan. IL NUOVO CEMENTO, 15 C.
Bartesaghi-Koc, C., Haddad, S., Pignatta, G., Paolini, R., Prasad, D., Santamouris, M., 2021. Can urban heat be mitigated in a single urban street? Monitoring, strategies, and performance results from a real scale redevelopment project. Sol. Energy 216, 564–588. https://doi.org/10.1016/j.solener.2020.12.043.
Borghi, S., Corbetta, G., De Biase, L., 2000. A Heat Island Model for Large Urban Areas and Its Application to Milan (*), vol. 23.
Bowler, D.E., Buyung-Ali, L., Knight, T.M., Pullin, A.S., 2010. Urban greening to cool towns and cities: a systematic review of the empirical evidence. Landsc. Urban Plan. 97 (3), 147–155. https://doi.org/10.1016/j.landurbplan.2010.05.006.
Bruse, M., 2004. ENVI-met 3.0: Updated Model Overview. www.envi-met.com.
Bruse, M., Fleer, H., 1998. Simulating surface–plant–air interactions inside urban environments with a three dimensional numerical model. Environ. Model. Softw. 13 (3–4), 373–384. https://doi.org/10.1016/S1364-8152(98)00042-5.
Castaldo, V.L., Pisello, A.L., Pigliautile, I., Piselli, C., Cotana, F., 2017. Microclimate and air quality investigation in historic hilly urban areas: experimental and numerical investigation in central Italy. Sustain. Cities Soc. 33, 27–44. https://doi.org/10.1016/j.scs.2017.05.017.
Ciacci, C., Banti, N., Di Naso, V., Bazzocchi, F., 2023. Green strategies for improving urban microclimate and air quality: a case study of an Italian industrial district and facility. Build. Environ. 244. https://doi.org/10.1016/j.buildenv.2023.110762.
Crank, P.J., Sailor, D.J., Ban-Weiss, G., Taleghani, M., 2018. Evaluating the ENVI-met microscale model for suitability in analysis of targeted urban heat mitigation strategies. Urban Clim. 26, 188–197. https://doi.org/10.1016/j.uclim.2018.09.002.
Datcu, S., Ibos, L., Candau, Y., Matteï, S., 2005. Improvement of building wall surface temperature measurements by infrared thermography. Infrared Phys. Technol. 46 (6), 451–467. https://doi.org/10.1016/j.infrared.2005.01.001.
De Ridder, K., Lauwaet, D., Maiheu, B., 2015. UrbClim – a fast urban boundary layer climate model. Urban Clim. 12, 21–48. https://doi.org/10.1016/j.uclim.2015.01.001.
Detommaso, M., Costanzo, V., Nocera, F., 2021. Application of weather data morphing for calibration of urban ENVI-met microclimate models. Results and critical issues. Urban Clim. 38. https://doi.org/10.1016/j.uclim.2021.100895.
Eingrüber, N., Domm, A.S., Korres, W., Schneider, K., 2024. Simulation of the Heat Mitigation Potential of Unsealing Measures in Cities by Parameterizing Grass Grid Pavers for Urban Microclimate Modelling With ENVI-met (V5). https://doi.org/10.5194/egusphere-2024-697.
Gagge, A.P.J.A.S., Nishi, Y., 1972. An effective temperature scale based on a simple model of human physiological regulatiry response. Mem. Faculty Eng. Hokkaido Univ. 13 (Suppl), 21–36.
Gao, K., Haddad, S., Paolini, R., Feng, J., Altheeb, M., Al Mogirah, A., Moammar, A.B., Santamouris, M., 2024. The use of green infrastructure and irrigation in the mitigation of urban heat in a desert city. Build. Simul. 17 (5), 679–694. https://doi.org/10.1007/s12273-024-1110-0.
Giorio, M., Paparella, R., 2023. Climate mitigation strategies: the use of cool pavements. Sustainability 15 (9). https://doi.org/10.3390/su15097641.
Han, D., Zhang, T., Qin, Y., Tan, Y., Liu, J., 2023. A comparative review on the mitigation strategies of urban heat island (UHI): a pathway for sustainable urban development. Clim. Dev. 15 (5), 379–403. Taylor and Francis Ltd. https://doi.org/10.1080/17565529.2022.2092051.
Huizenga, C., Hui, Z., Arens, E., 2001. A model of human physiology and comfort for assessing complex thermal environments. Build. Environ. 36 (6), 691–699. https://doi.org/10.1016/S0360-1323(00)00061-5.
Huttner, 2012. Further Development and Application of the 3D Microclimate Simulation ENVI-Met.
ISPRA, 2023. Ambiente in Italia: uno sguardo d'insieme. Annuario dei dati ambientali 2022. Istituto Superiore per la Protezione e la Ricerca Ambientale, oma. https://indicatoriambientali.isprambiente.it.
Jing, W., Qin, Z., Mu, T., Ge, Z., Dong, Y., 2024. Evaluating thermal comfort indices for outdoor spaces on a university campus. Sci. Rep. 14 (1), 21253.
Kottek, M., Grieser, J., Beck, C., Rudolf, B., Rubel, F., 2006. World Map of the Köppen-Geiger climate classification updated. Meteorol. Z. 15 (3), 259–263. https://doi.org/10.1127/0941-2948/2006/0130.
Krayenhoff, E.S., Broadbent, A.M., Zhao, L., Georgescu, M., Middel, A., Voogt, J.A., Martilli, A., Sailor, D.J., Erell, E., 2021. Cooling hot cities: a systematic and critical review of the numerical modelling literature. Environ. Res. Lett. 16 (5), 053007. https://doi.org/10.1088/1748-9326/abdcf1.
Lee, J., Zhang, H., Arens, E., 2013. UC Berkeley Indoor Environmental Quality (IEQ) Title Typical Clothing Ensemble Insulation Levels for Sixteen Body Parts. http://escholarship.org/uc/item/18f0r375.
Lindberg, F., Holmer, B., Thorsson, S., 2008. SOLWEIG 1.0 – Modelling spatial variations of 3D radiant fluxes and mean radiant temperature in complex urban settings. Int. J. Biometeorol. 52 (7), 697–713. https://doi.org/10.1007/s00484-008-0162-7.
Lobaccaro, G., De Ridder, K., Acero, J.A., Hooyberghs, H., Lauwaet, D., Maiheu, B., Sharma, R., Govehovitch, B., 2021. Applications of models and tools for mesoscale and microscale thermal analysis in mid-latitude climate regions—a review. Sustainability 13 (22). https://doi.org/10.3390/su132212385. MDPI.
Maronga, B., Banzhaf, S., Burmeister, C., Esch, T., Forkel, R., Fröhlich, D., Fuka, V., Gehrke, K.F., Geletič, J., Giersch, S., Gronemeier, T., Groß, G., Heldens, W., Hellsten, A., Hoffmann, F., Inagaki, A., Kadasch, E., Kanani-Sühring, F., Ketelsen, K., Raasch, S., 2020. Overview of the PALM model system 6.0. Geosci. Model Dev. 13 (3), 1335–1372. https://doi.org/10.5194/gmd-13-1335-2020.
Matzarakis, A., Rutz, F., Mayer, H., 2007. Modelling radiation fluxes in simple and complex environments—application of the RayMan model. Int. J. Biometeorol. 51 (4), 323–334. https://doi.org/10.1007/s00484-006-0061-8.
Matzarakis, A., Rutz, F., Mayer, H., 2010. Modelling radiation fluxes in simple and complex environments: basics of the RayMan model. Int. J. Biometeorol. 54 (2), 131–139. https://doi.org/10.1007/s00484-009-0261-0.
Mendes, P.T., Nouri, A.S., Matzarakis, A., 2025. Evaluating outdoor human thermal comfort through climate-resilient adaptation: a case study at school of science and technology (NOVA FCT) campus. Atmosphere 16 (6), 677.
Meng, F., Qin, M., Gao, Z., Wang, H., Xu, X., Xu, F., 2025. A review of RayMan in thermal comfort simulation: development, applications and prospects. Build. Environ. 270, 112547. https://doi.org/10.1016/j.buildenv.2025.112547.
Middel, A., Häb, K., Brazel, A.J., Martin, C.A., Guhathakurta, S., 2014. Impact of urban form and design on mid-afternoon microclimate in Phoenix Local Climate Zones. Landsc. Urban Plan. 122, 16–28. https://doi.org/10.1016/j.landurbplan.2013.11.004.
Mineo, S., Pappalardo, G., 2021. Rock emissivity measurement for infrared thermography engineering geological applications. Appl. Sci. 11 (9). https://doi.org/10.3390/app11093773.
Nagy, L.D.F., 2004. EUFORGEN Technical Guidelines for Genetic Conservation and Use for Field Maple (Acer campestre).
Ng, E.R.C., 2015. In: Ren, C. (Ed.), The Urban Climatic Map: A Methodology for Sustainable Urban Planning. Routledge.
Oke, T.R., 1982. The energetic basis of the urban heat island. Q. J. R. Meteorol. Soc. 108 (455), 1–24. https://doi.org/10.1002/qj.49710845502.
Oke, T.R., 2002. Boundary Layer Climates, 2nd ed. Taylor and Francis e-Library. British Library Cataloguing in Publication Data.
Olivieri, F., Sassenou, L.-N., Olivieri, L., 2024. Potential of nature-based solutions to diminish urban heat island effects and improve outdoor thermal comfort in summer: case study of Matadero Madrid. Sustainability 16 (7), 2778. https://doi.org/10.3390/su16072778.
Peel, M.C., Finlayson, B.L., McMahon, T.A., 2007. Updated world map of the Köppen-Geiger climate classification. Hydrol. Earth Syst. Sci. 11 (5), 1633–1644. https://doi.org/10.5194/hess-11-1633-2007.

Perini, K., Magliocco, A., 2014. Effects of vegetation, urban density, building height, and atmospheric conditions on local temperatures and thermal comfort. Urban Forest. Urban Green. 13 (3), 495–506. https://doi.org/10.1016/j.ufug.2014.03.003.
Pichierri, M., Bonafoni, S., Biondi, R., 2012. Satellite air temperature estimation for monitoring the canopy layer heat island of Milan. Remote Sens. Environ. 127, 130–138. https://doi.org/10.1016/j.rse.2012.08.025.
Piselli, C., Castaldo, V.L., Pigliautile, I., Pisello, A.L., Cotana, F., 2018. Outdoor comfort conditions in urban areas: on citizens' perspective about microclimate mitigation of urban transit areas. Sustain. Cities Soc. 39, 16–36. https://doi.org/10.1016/j.scs.2018.02.004.
Podaras, P.B.N., 1996. The propagation of lesser known and unusual maple species. In: Combined Proceedings International Plant Propagator's Society, pp. 497–507.
Puche, M., Vavassori, A., Brovelli, M.A., 2023. Insights into the effect of urban morphology and land cover on land surface and air temperatures in the metropolitan city of Milan (Italy) using satellite imagery and in situ measurements. Remote Sens. 15 (3). https://doi.org/10.3390/rs15030733.
Rosso, F., Golasi, I., Castaldo, V.L., Piselli, C., Pisello, A.L., Salata, F., Ferrero, M., Cotana, F., de Lieto Vollaro, A., 2018. On the impact of innovative materials on outdoor thermal comfort of pedestrians in historical urban canyons. Renew. Energy 118, 825–839. https://doi.org/10.1016/j.renene.2017.11.074.
Salata, F., Golasi, I., de Lieto Vollaro, R., de Lieto Vollaro, A., 2016. Urban microclimate and outdoor thermal comfort. A proper procedure to fit ENVI-met simulation outputs to experimental data. Sustain. Cities Soc. 26, 318–343. https://doi.org/10.1016/j.scs.2016.07.005.
Salata, F., Golasi, I., Petitti, D., de Lieto Vollaro, E., Coppi, M., de Lieto Vollaro, A., 2017. Relating microclimate, human thermal comfort and health during heat waves: an analysis of heat island mitigation strategies through a case study in an urban outdoor environment. Sustain. Cities Soc. 30, 79–96. https://doi.org/10.1016/j.scs.2017.01.006.
Santamouris, M., 2013. Using cool pavements as a mitigation strategy to fight urban heat island—a review of the actual developments. Renew. Sust. Energ. Rev. 26, 224–240. https://doi.org/10.1016/j.rser.2013.05.047.
Santamouris, M., 2020. Recent progress on urban overheating and heat island research. Integrated assessment of the energy, environmental, vulnerability and health impact. Synergies with the global climate change. In: Energy and Buildings, vol. 207. Elsevier Ltd. https://doi.org/10.1016/j.enbuild.2019.109482
Skamarock, W.C., K. J. B., 2024. Weather Research and Forecasting (WRF) Model. National Center for Atmospheric Research (NCAR).
Song, B., Park, K., 2015. Contribution of greening and high-albedo coatings to improvements in the thermal environment in complex urban areas. Adv. Meteorol. 2015. https://doi.org/10.1155/2015/792172.
Stolwijk, J.A.J., Hardy, J.D., 1966. Temperature regulation in man? A theoretical study. Pflug. Arch. Gesamte Physiol. Menschen Tiere 291 (2), 129–162. https://doi.org/10.1007/BF00412787.
Toparlar, Y., Blocken, B., Maiheu, B., van Heijst, G.J.F., 2017. A review on the CFD analysis of urban microclimate. Renew. Sust. Energ. Rev. 80, 1613–1640. https://doi.org/10.1016/j.rser.2017.05.248.
Tsoka, S., Tsikaloudaki, K., Theodosiou, T., 2017. Urban space's morphology and microclimatic analysis: a study for a typical urban district in the Mediterranean city of Thessaloniki, Greece. Energ. Buildings 156, 96–108. https://doi.org/10.1016/j.enbuild.2017.09.066.
Tsoka, S., Tsikaloudaki, A., Theodosiou, T., 2018. Analyzing the ENVI-met microclimate model's performance and assessing cool materials and urban vegetation applications–a review. In: Sustainable Cities and Society, vol. 43. Elsevier Ltd., pp. 55–76. https://doi.org/10.1016/j.scs.2018.08.009
Vieira Zezzo, L., Pereira Coltri, P., Dubreuil, V., 2023. Microscale models and urban heat island studies: a systematic review. Environ. Monit. Assess. 195 (11). https://doi.org/10.1007/s10661-023-11906-2. Springer Science and Business Media Deutschland GmbH.
Vogel, J., Afshari, A., Chockalingam, G., Stadler, S., 2022. Evaluation of a novel WRF/PALM-4U coupling scheme incorporating a roughness-corrected surface layer representation. Urban Clim. 46. https://doi.org/10.1016/j.uclim.2022.101311.
Vollmer, M., Mollmann, K.-P., 2008. Survey of optical systems. In: Handbook of Optical Systems, vol. 4. Wiley-VCH.
Yang, X., Zhao, L., Bruse, M., Meng, Q., 2013. Evaluation of a microclimate model for predicting the thermal behavior of different ground surfaces. Build. Environ. 60, 93–104. https://doi.org/10.1016/j.buildenv.2012.11.008.
Zhang, H., Arens, E., Huizenga, C., Han, T., 2010a. Thermal sensation and comfort models for non-uniform and transient environments: part I: local sensation of individual body parts. Build. Environ. 45 (2), 380–388. https://doi.org/10.1016/j.buildenv.2009.06.018.
Zhang, H., Arens, E., Huizenga, C., Han, T., 2010b. Thermal sensation and comfort models for non-uniform and transient environments, part II: local comfort of individual body parts. Build. Environ. 45 (2), 389–398. https://doi.org/10.1016/j.buildenv.2009.06.015.
Zhang, H., Arens, E., Huizenga, C., Han, T., 2010c. Thermal sensation and comfort models for non-uniform and transient environments, part III: whole-body sensation and comfort. Build. Environ. 45 (2), 399–410. https://doi.org/10.1016/j.buildenv.2009.06.020.